Differences in aerosol and cloud properties along the central California coast when winds change from northerly to southerly

Kira Zeider[1], Grace Betito[2], Anthony Bucholtz[3], Peng Xian[4], Annette Walker[4], Armin Sorooshian[1,2*]

[1]Department of Chemical and Environmental Engineering, University of Arizona, Tucson, Arizona, 85721, USA
[2]Department of Hydrology and Atmospheric Sciences, University of Arizona, Tucson, Arizona, 85721, USA
[3]Department of Meteorology, Naval Postgraduate School, Monterey, California, 93943, USA
[4]Marine Meteorology Division, Naval Research Laboratory, Monterey, California, 93943, USA

*Correspondence to: Armin Sorooshian (armin@arizona.edu)

Abstract. Wind reversals resulting in southerly flow along the California coast are not well understood in terms of how aerosol and cloud characteristics change. This gap is addressed using airborne field measurements enhanced with data from space-borne remote sensing (Moderate Resolution Imaging Spectroradiometer), surface stations (Interagency Monitoring of Protected Visual Environments), and models (Navy Aerosol Analysis and Prediction System and Coupled Ocean/Atmosphere Mesoscale Prediction System), with a focus on sub- and supermicron aerosol, and cloud microphysical variables: cloud droplet number concentration (N_d), cloud optical thickness (COT), and cloud droplet effective radius (r_e). Southerly flow coincided with higher values of submicron aerosol concentration (N_a) and mass concentrations of species representative of fine aerosol pollution (NO_3^- and nss-SO_4^{2-}) and shipping/continental emissions (V, oxalate, NH_4^+, Ni, OC, and EC). Supermicron N_a did not change, however, heightened levels of acidic species in southerly flow coincided with reduced Cl^-:Na^+ suggestive of Cl^- depletion in salt particles. Clouds responded correspondingly in southerly flow, with more acidic cloud water, higher levels of similar species as in the aerosol phase (e.g., NO_3^-, nss-SO_4^{2-}, NH_4^+, V), along with elevated values of N_d and COT and reduced r_e during campaigns with similar cloud liquid water paths. Case study flights help to visualize offshore pollution gradients and highlight the sensitivity of the results to the presence of widespread smoke coverage including how associated plumes have enhanced supermicron N_a. These results have implications for aerosol-cloud interactions during wind reversals, and have relevance for weather, public welfare, and aviation.

1 Introduction

The northeastern Pacific Ocean is one of the most heavily studied regions as it relates to aerosol-cloud interactions due to the persistent and spatially broad stratocumulus cloud deck that is influenced by a variety of emissions sources, notably shipping (Wood, 2012; Russell et al., 2013). One aspect of that region that warrants more attention is the predominant direction of lower tropospheric winds, as recent work has suggested that it can have significant implications for aerosol and cloud properties (Juliano et al., 2019a; 2019b; Juliano and Lebo, 2020). The wind direction along the North American west coast is influenced by its topography, namely the coastal mountains (e.g., National Research Council, 1992), and during the California (CA) warm season (April through September) it is primarily from the north along the coast. An important weather phenomenon during that season is the infrequent and short-lived (from one to several days) transition from northerly to southerly flow near the coast up to 100 km offshore (e.g., Nuss et al., 2000). Particularly, the northerly winds weaken (e.g., Winant et al., 1987; Melton et al., 2009) and eventually reverse. Along with a decrease in temperature and increases in pressure and cloud fraction (e.g., increases in low clouds and fog), there is also a change in overall wind speed: most northerlies (~75%) have a wind speed component less than 5 m s^{-1} (Bond et al., 1996), whereas southerly "surges" are characterized by sudden increases in wind speed to 15 m s^{-1} or greater (Mass and Albright, 1987). This is not a phenomenon that is unique to the U.S.; a handful of studies have noted these events along the coasts of South America (e.g., Garreaud et al., 2002; Garreaud and Rutllant, 2003), southern Africa (e.g., Reason and Jury, 1990), and even Australia (e.g., Holland and Leslie, 1986; Reason et al., 1999; Reid and Leslie, 1999).

These wind reversals – referred to as either coastally trapped disturbances (CTDs), coastally trapped wind reversals (CTWRs), stratus surges, or southerly surges, to name a few – have been studied since the 1970s (Gill, 1977; Dorman, 1985). There have been a fair number of publications discussing the dynamics and forcing mechanisms for such events (thoroughly reviewed by Nuss et al., 2000) primarily using data from buoys, radars, and research aircraft. Buoy (e.g., Bond et al., 1996) and satellite studies (e.g., Parish, 2000; Rahn and Parish, 2010) mainly discussed the topics related to mesoscale structure, while the research aircraft studies (e.g., Ralph et al., 1998; Rahn and Parish, 2007) have attempted to document physical characteristics of the wind reversal. For example, Rahn and Parish (2007) used sawtooth maneuvers to depict the vertical structure of the 22-25 June 2006 reversal through examining surface pressure, temperature, wind direction, wind speed, along-shore wind, and cross-shore wind. Additionally, there have been multiple studies attempting to model these wind reversals (e.g., Rogerson and Samelson, 1995; Guan et al., 1998; Skamarock et al., 1999; Mass and Steenburgh, 2000; Thompson et al., 2005) to better understand their initiation, propagation, and cessation. These studies found that CTDs are initiated by changes in synoptic-scale flow, particularly offshore, and that the coastal mountains dampen the flow, deepen the marine layer, and propagate a mesoscale coastal ridge of higher pressure northward that ultimately leads to the development of a coastally trapped southerly wind component.

However, there have been limited attempts to look into aerosol and cloud characteristics during a southerly surge (e.g., Juliano et al., 2019a; 2019b), and among them were studies that happened to encounter them by chance without these surges having been the study's focus (Crosbie et al., 2016; Dadashazar et al., 2020). Juliano et al. (2019a) was, to our best knowledge, the first study to focus on CTD aerosol-cloud interactions using 23 cases identified between 2004 and 2016 with buoy data and satellite imagery. They found notable differing characteristics between non-CTD (northerly flow) and CTD (southerly flow) conditions, with higher cloud droplet number concentration (N_d) and lower droplet effective radius (r_e) for CTD cases. Compared to non-CTD events, CTD events had r_e values that were ~20-40% lower (i.e., differences often exceeding ~3 µm) and N_d values (~250 cm^{-3}) that were almost twice as large in many areas. They attributed this to some combination of (i) mixing of sea salt particles into the boundary layer due to an observed wind stress-sea surface temperature cycle; (ii) offshore flow transporting continental aerosol into areas offshore of CA; and (iii) extended periods of time that southerly air spends in shipping lanes. Some continental sources they noted include agricultural emissions from the CA Central Valley, biogenic emissions from various major sources such as forests around Oregon and northern CA, smoke from biomass burning, and urban emissions from major CA cities such as Los Angeles, San Jose, Sacramento, and San Francisco. These sources have been confirmed in various studies conducted in coastal areas of central CA (Wang et al., 2014; Maudlin et al., 2015; Braun et al., 2017; Dadashazar et al., 2019; Ma et al., 2019). A subsequent study (Juliano et al., 2019b) analyzed three CTD events using satellite and aircraft observations, as well as numerical simulations. That study's usage of aircraft data was limited to cloud water composition, to support results from their previous study that non-CTD days were primarily influenced by marine sources like sea salt, whereas CTD days exhibited more relative influence from continental and shipping

84   (i.e., higher SO_4^{2-} and NO_3^-) sources. Those studies noted that additional observations, specifically of an in situ nature,
85   were needed to confirm results that were mostly based on modeling and remote sensing.
86   The goal of this study is to contrast aerosol and cloud characteristics between southerly and northerly flow
87   regimes in the lower troposphere (below 3 km) offshore of central CA. Note that this study's primary objective is not
88   to characterize meteorological and large-scale features associated with wind reversals and we do not classify events
89   based on whether they are CTDs but rather categorize events based on boundary layer wind direction. As a way to
90   address the shortage of in situ observational data used for this research application, an important inventory of airborne
91   data is leveraged that have been collected over the last two decades (Sorooshian et al., 2018) that afford increased
92   sampling density of southerly flow cases relative to Juliano et al. (2019b). Such cases are difficult to sample owing to
93   their lower frequencies (Table 1) compared to days with northerly flow and because aircraft flights do not occur each
94   day, so some southerly cases are missed during airborne campaigns. In total, 17 days of data exist from Naval
95   Postgraduate School (NPS) Twin Otter campaigns coinciding with southerly flow, with some days including multiple
96   flights. One thing that has yet to happen in past studies is to use in situ data to compare more than just cloud water
97   composition but also relevant variables such as aerosol number concentration (N_a) and N_d, which is crucial to
98   intercompare with satellite data and put previous speculations about aerosol and cloud responses to southerly flow on
99   sturdier ground. As the aircraft data are still limited, we complement the analysis with other datasets, including those
100 from satellite remote sensors, models, and surface stations.
101   The structure of this paper is as follows: Sect. 2 reports on methods used; Sect. 3 shows results beginning
102 with a discussion of how well a model can represent southerly winds, followed by assessing how well the datasets
103 show more fine pollution during southerly days and if clouds respond accordingly with the usual chain of events
104 associated with the Twomey effect (Twomey, 1974) whereby clouds have more but smaller drops at similar liquid
105 water path; and Sect. 4 provides conclusions. The results of this work have implications for numerous societal and
106 environmental factors sensitive to aerosol and cloud characteristics such as transportation (especially aviation),
107 agriculture, biogeochemical cycling of nutrients and contaminants, and coastal ecology (Dadashazar et al., 2020).
108
109 **2   Methods**
110   This study relies on the use of multiple datasets to examine how aerosol and cloud characteristics vary
111 between traditional northerly flow along the CA coastline as compared to less common southerly flow periods. This
112 study was initially inspired by airborne field measurements (Table 1) whereby on a few opportune flight days,
113 southerly flow was encountered off the CA coast. Because these events were rare in comparison to the majority of
114 flights with northerly flow (Southerly Winds % in Table 1), several campaigns worth of data are compiled to increase
115 data points for southerly flow days. The airborne data used here are all from summer periods, which is when most
116 field studies have focused on this region to investigate aerosol-cloud interactions (e.g., Russell et al., 2013) allowing
117 for easier intercomparison for interested readers. We enhance data volume by also conducting complementary
118 analyses with data obtained from spaceborne remote sensing, surface-based stations, and models. Below we first
119 describe the airborne datasets, followed by the wind classification method, and then descriptions of the models, surface
120 data, and satellite data.
121
122 **2.1   Airborne Field Missions**
123   This study utilizes data from six airborne missions based out of Marina, CA (white diamond; Fig. 1) using
124 the Naval Postgraduate School (NPS) Twin Otter aircraft. Marina is approximately 5 km away from the coastline. The
125 scientific target of these campaigns included a mix of aerosol-cloud interactions, aerosol microphysical processes, and
126 characterization of wildfire emissions: the Eastern Pacific Emitted Aerosol Cloud Experiment (E-PEACE), the
127 Nucleation in California Experiment (NiCE), the Biological and Oceanic Atmospheric Study (BOAS), the Fog and
128 Stratocumulus Evolution Experiment (FASE), the Marine Aerosol Cloud And Wildfire Study (MACAWS), and the
129 California Smoke Mission (CSM) (Table 1). Another Twin Otter mission from 2019 (Monterey Aerosol Research
130 Campaign - MONARC) is not included in this analysis due to the lack of southerly flow days sampled during the
131 campaign. The research flight (RF) paths for each campaign are shown in Fig. 1. In some instances, multiple flights
132 were conducted on a single day, either to capture time-sensitive atmospheric features or to collect data beyond the
133 endurance limit of the instrumented aircraft. For those days, RFs are assigned the same number but are distinguished
134 with endings 'A,' 'B,' and 'C,' for successive flights, respectively. E-PEACE and NiCE had the most cases of
135 southerly flow owing partly to those campaigns having had the most flights: five out of 30 flights for E-PEACE; four

136 out of 23 flights for NiCE. BOAS also had four flights with southerly flow (out of 15 flights), but they were spread
137 across two flights days as compared to E-PEACE and NiCE whose southerly flights were all on distinct days.
138    The Twin Otter flew at ~55 m s^{-1} and conducted measurements during level legs and sounding profiles, over
139 both the land and the ocean, and within and above the boundary layer during flight periods ranging from one to five
140 hours. Additional information regarding aircraft and flight characteristics, as well as the general flight strategy is
141 summarized in Sorooshian et al. (2019). The general area of focus in this study was within the following range of
142 coordinates, with many of the results specifically targeting just the ocean areas in this spatial domain: 35.31° N –
143 40.99° N, 125.93° W – 118.98° W.
144    This study's analysis focuses on maximizing the number of southerly and northerly cases available from the
145 flight data rather than keeping a similar number of flights to represent southerly and northerly conditions. The rationale
146 to include all available northerly flight days (which exceed southerly days; Table 1) is that their combined use is more
147 representative of typical northerly conditions and less sensitive to inter-day variations. That being said, a random
148 selection of northerly flight days was still used to compare to the more limited number of southerly flight days (not
149 shown here), with the same general conclusions reached as compared to using all northerly flight days.
150
151 **Table 1: Summary of NPS Twin Otter campaigns used in this study, including dates, number of RFs per campaign, RFs**
152 **that are categorized as having had southerly flow, and percentage of southerly days during the campaign period (including**
153 **all days in those months and not just RF days). Days are categorized as having southerly flow based on the analysis in Sect.**
154 **2.2.**

Campaign	Dates	Total RFs	RF # (Flight Date) with Southerly Winds	Southerly Winds % (# Southerly days / Total days in period)
E-PEACE	07/08 – 08/18/2011	30	RF11 (07/23), RF12 (07/24), RF14 (07/27), RF15 (07/28), RF16 (07/29)	12.90% (8/62)
NiCE	07/08 – 08/07/2013	23	RF7 (07/16), RF8 (07/17), RF9 (07/18), RF16 (07/29)	14.52% (9/62)
BOAS	07/02 – 07/24/2015	15	RF10A & 10B (07/16), RF11A & 11B (07/17)	32.26% (10/31)
FASE	07/18 – 08/12/2016	16	RF6A, 6B, & 6C (07/29)	14.52% (9/62)
MACAWS	06/21 – 07/12/2018	16	RF12 (07/05), RF16 (07/12)	4.92% (3/61)
CSM	09/01 – 09/25/2020	14	RF1 (09/01), RF5 (09/09), RF6 (09/10)	13.33% (4/30)

155
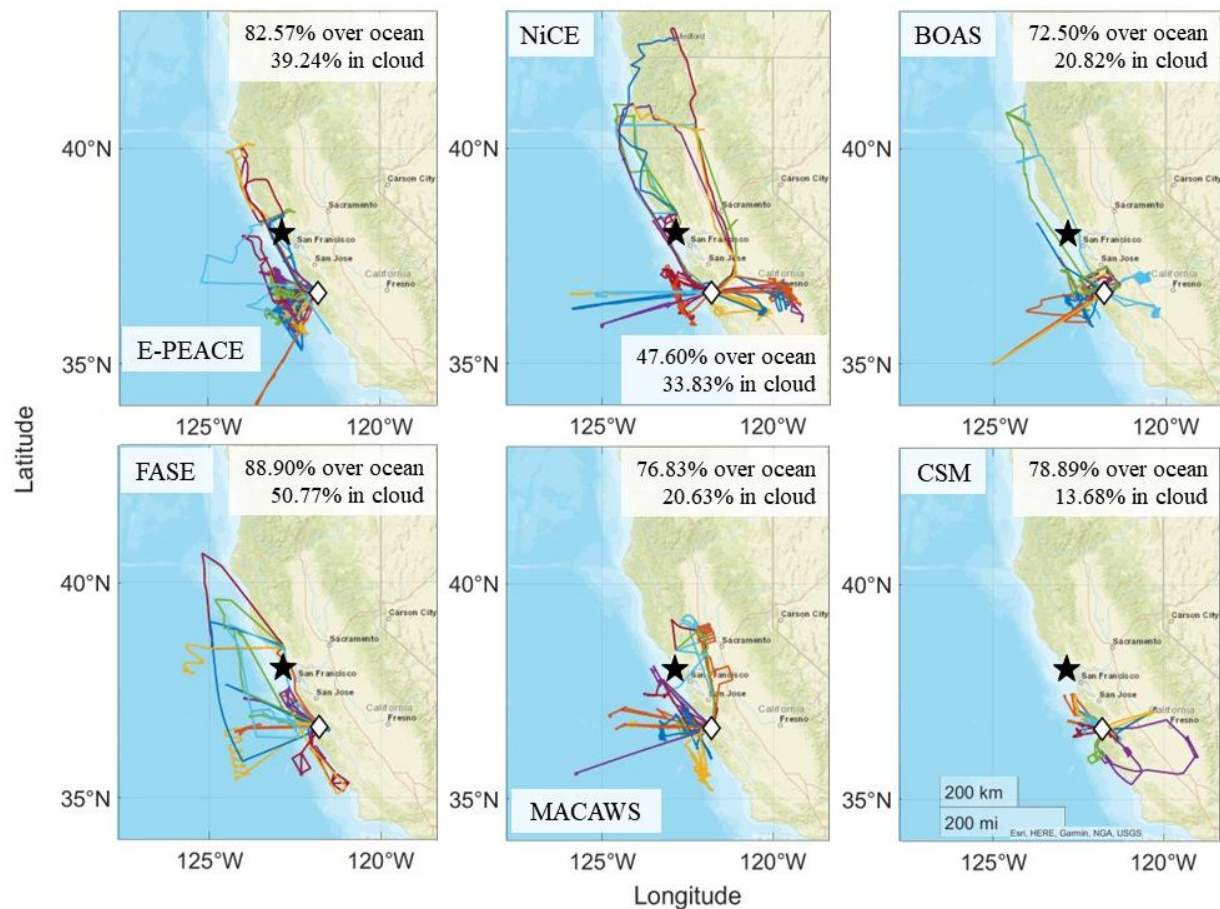
Figure 1: Research flight paths for the six Twin Otter campaigns used in this study. The aircraft base at Marina, CA is denoted by a white diamond, and the IMPROVE station used in this study is indicated by a black star (Pt. Reyes National Seashore). The legends in each panel report on the percentage of flight time spent over the ocean and in cloud over the ocean.

2.1.1   Twin Otter Instrumentation

Table 2 summarizes the relevant instruments used for each Twin Otter mission pertinent to this work. More extensive details about the instruments, and those not listed below such as relevant navigational and meteorological instruments, are described in Sorooshian et al. (2018).

Table 2: Summary of Twin Otter payload during the field campaigns used for this study. The six farthest right columns show instrument availability for each campaign.

Instrument	Measured variable	Size range	Time resolution	E-PEACE	NiCE	BOAS	FASE	MACAWS	CSM
TSI Ultra-fine Condensation Particle Counter (CPC) 3025	$N_{a>3nm}$	> 0.003 µm	1 s	X	X	X	X	X	X
TSI Condensation Particle Counter (CPC) 3010	$N_{a>10nm}$	> 0.01 µm	1 s	X	X	X	X	X	X

Instrument	Variable	Size range	Time resolution						
PMS/DMT Passive Cavity Aerosol Spectrometer Probe (PCASP)	$N_{a0.1\text{-}1\mu m}$, $N_{a>1\mu m}$	~0.1 – 3.4 µm	1 s	X	X	X	X	X	X
DMT Cloud and Aerosol Spectrometer - Forward Scattering (CASF)	N_d	~0.6 - 60 µm	1 s	X	X		X	X	X
PMS/DMT Forward Scattering Spectrometer Probe (FSSP)	N_d	1 - 46 µm	1 s		X	X	X	X	
ARI Aerosol Mass Spectrometer (AMS)	Speciated mass conc.	~60 - 600 nm	< 15 s	X	X	X			
Mohnen Cloud Water Collector - pH, IC, ICPMS	pH, air-equivalent mass conc.	N/A	~ 5 - 60 min	X	X	X	X	X	

Condensation particle counters (CPCs; TSI, Inc.) were used to measure particle number concentrations for diameters greater than 3 ($N_{a>3nm}$ or N_{a3}) and 10 nm ($N_{a>10nm}$ or N_{a10}), respectively, as well as the Passive Cavity Aerosol Spectrometer Probe (PCASP; Particle Measuring Systems (PMS), Inc., modified by Droplet Measurement Technologies (DMT), Inc.) for diameters between ~100 nm and 3.4 µm. The Cloud and Aerosol Spectrometer – Forward Scattering (CASF; DMT, Inc.) measured the size distribution of larger particles and droplets between 0.6 – 60 µm for all missions except for BOAS when the Forward Scattering Spectrometer Probe (FSSP; PMS, Inc. modified by DMT, Inc.) was used in its place. The cloud probes were calibrated before each field campaign to ensure consistency between the instruments (Sorooshian et al., 2018). The CASF and FSSP size distributions were integrated to determine total N_d and liquid water content (LWC) when the aircraft was in cloud using the criterion of LWC >0.02 g m^{-3}; all instances of LWC <0.02 g m^{-3} were considered cloud-free and only considered for quantification of aerosol variables such as total N_a in different size ranges (Fig. S1). Additionally, RFs categorized as southerly flow were filtered to only include data during periods when the horizontal wind direction was between 135° and 225°. A variety of statistics were calculated for the reported and derived variables (e.g., $N_{a>3nm}$, $N_{a>10nm}$, $N_{a10\text{-}100nm}$ ($N_{a>10nm}$ - $N_{a0.1\text{-}1\mu m}$), $N_{a0.1\text{-}1\mu m}$, $N_{a>1\mu m}$, the ratio of N_{a3} to N_{a10} ($N_{a3}:N_{a10}$), N_d, horizontal wind speed and direction) in categories of interest including medians and minimum/maximum values. The mode wind direction was calculated for each RF as well as each overall campaign, since that statistic is assumed here to be a better representation of typical wind directions rather than the median.

An Aerosol Mass Spectrometer (AMS; Aerodyne Research Inc. (ARI)) was used during some campaigns to measure sub-micrometer (submicron) aerosol composition, specifically for non-refractory components (SO_4^{2-}, NO_3^-, NH_4^+, Cl^-, and organics). Coggon et al. (2012; 2014) discuss in detail the AMS operational details and results from some of the campaigns. Cloud water (CW) was collected using a Mohnen CW collector, which was manually placed above the fuselage of the Twin Otter during cloud penetrations for sample collection into vials kept inside the aircraft. After flights, samples were analyzed for pH and speciated concentrations of various water-soluble ions and elements, with a number of studies summarizing the operational details and selected results (e.g., Wang et al., 2014; Wang et al., 2016; MacDonald et al., 2018). An Oakton Model 110 pH meter was used for E-PEACE, NiCE, and BOAS, and a Thermo Scientific Orion 8103BNUWP Ross Ultra Semi-Micro pH probe was used for FASE and MACAWS. Water-soluble ionic composition was measured via Ion Chromatography (IC; Thermo Scientific Dionex ICS – 2100 system), except some ions during E-PEACE, including Na^+, could not be measured. Water-soluble elemental composition was measured via Inductively Coupled Plasma Mass Spectrometry (ICP-MS; Agilent 7700 Series) for E-PEACE, NiCE, and BOAS, and via Triple Quadrupole Inductively Coupled Plasma Mass Spectrometry (ICP-QQQ; Agilent 8800 Series) for FASE and MACAWS. Cloud water was not collected during CSM. The IC species analyzed in this study are Cl^-, NH_4^+, NO_3^-, non-sea salt (nss)-SO_4^{2-}, and oxalate, and the ICPMS species analyzed are Ca^{2+}, K^+, Na^+, and V.

202 We used the following equation to calculate nss-SO_4^{2-} under the assumption that all Na^+ is from sea salt (e.g.,
203 AzadiAghdam et al., 2019):

205 $$[nss - SO_4^{2-}] = [SO_4^{2-}] - 0.253 \times [Na^+] \qquad (1)$$

207 Aqueous concentrations of ions and elements were converted into air-equivalent concentrations using the mean LWC
208 encountered when the aircraft was in cloud (LWC > 0.02 g m^{-3}) during collection of individual samples.
209 Aircraft data were analyzed four different ways over the study domain. The primary focus of the analysis is
210 using data within the spatial domain listed in Sect. 2.1 only when the aircraft was over the ocean (Fig 1). In addition
211 to a LWC maximum of 0.02 g m^{-3}, another screening criterion was utilized to omit data during RFs strongly influenced
212 by wildfire emissions (Table 3), which was when the median flight-wide $N_{a>10nm}$ value exceeded 7,000 cm^{-3} for
213 altitudes less than 800 m. This value was determined by closely examining flights that flew through areas with reported
214 wildfire influence using flight notes. Data were alternatively analyzed for RF segments only over the ocean without
215 the $N_{a>10nm}$ criterion applied, and then also when the aircraft flew within the spatial domain over land and ocean both
216 with and without the same wildfire criterion; those results are shown in Tables S1 - S3. Note that CSM was the only
217 campaign for which this criterion was not applied, as smoke was the sole focus of the mission and the flights are
218 considered to all have been influenced to some extent. Moreover, CSM is unique amongst the campaigns examined
219 where the scientific hypotheses to be tested are not as applicable due to the widespread smoke coverage, but we still
220 examine it as it can provide useful insights.
221 Mann-Whitney U tests were performed for the aircraft data and the CW data, where the null hypotheses (p ≤
222 0.05) were that the medians of certain variables (N_a, N_d, wind speed and direction) and species concentrations of
223 southerly and northerly wind days were similar within a campaign.

225 **2.2   Wind Direction Classification**
226 To determine boundary layer wind direction in the study region, we used a number of data products, as each
227 provided unique advantages either related to temporal, spatial, or vertical coverage. Data from NOAA's National Data
228 Buoy Center (NDBC) were analyzed to verify the ocean surface wind direction was between 135° and 225°, which is
229 considered southerly in this study. We focused on wind direction during 1400 - 2200 UTC to overlap with when the
230 majority of RFs occurred (Marina, CA is 7 hours behind UTC). Other days classified as northerly flow adhered to
231 surface wind direction between 315° and 45°. Five buoys were used to match the ones used in Juliano et al. (2019a):
232 46011 (Santa Maria: 34.94° N, 120.99° W), 46013 (Bodega Bay: 38.24° N, 123.32° W), 46014 (Point Arena: 39.23°
233 N, 123.98° W), 46028 (Cape San Martin: 35.77° N, 121.90° W), and 46042 (Monterey: 36.79° N, 122.40° W). Buoy
234 locations relative to the CA coast are shown in Fig. 1 of Juliano et al. (2019a).
235 The National Oceanic and Atmospheric Administration (NOAA) Hybrid Single-Particle Lagrangian
236 Integrated Trajectory (HYSPLIT; Stein et al., 2015; Rolph et al., 2017) model was used to obtain back trajectories
237 based on North American Mesoscale Forecast System (NAM) meteorological data (12 km resolution) ending at
238 Marina, CA (36.67° N, 121.60° W; white diamond in Fig. 1) for 500, 900, 2,500, and 4,500 m AGL. Marina, CA was
239 selected as the ending point for the back-trajectories as this was the takeoff/landing location for all six campaigns.
240 These altitudes were selected to both capture marine boundary layer (MBL) and free troposphere (FT) winds and
241 reflect the variety of altitudes the Twin Otter aircraft flew at during the six campaigns in Table 1; however, the
242 trajectories at 500 m were most important for connecting to the aircraft data analysis.
243 For Twin Otter flight days, aircraft wind data were used to confirm that wind direction was either southerly
244 or northerly in the lowest 800 m of the flights (over ocean and land), which was the altitude range of most of the flight
245 time. For a case-by-case basis, archived surface weather charts were accessed via the NOAA Weather Prediction
246 Center (WPC) to investigate wind direction at specific sites (like Pt. Reyes).
247 We also used Multi-Channel RGB data from the Geostationary Operational Environmental Satellite-WEST
248 Full Disk Cloud Product (GOES-15) to investigate cloud motion on northerly and southerly flow days. The analysis
249 utilized time resolutions of every three hours for E-PEACE, hourly for NiCE, BOAS, FASE, and MACAWS, and
250 every half-hour for CSM. We investigated all days within a campaign month, and not just days coinciding with a RF.
251 For example, E-PEACE comprised flights from 9 July to 18 August 2011, and thus GOES data from 1 July through
252 31 August 2011 were investigated for that year. While not an exact tracer for air motion, we did observe that clouds
253 tended to follow the prevalent air motion, particularly on southerly flow days.

2.3   NAAPS and COAMPS

Both the Navy Aerosol Analysis and Prediction System (NAAPS; Lynch et al., 2016; https://www.nrlmry.navy.mil/aerosol/) and the Coupled Ocean/Atmosphere Mesoscale Prediction System (COAMPS; Hodur, 1997) are used to support the analysis of airborne data collected during the six Twin Otter campaigns and assess how well they can simulate southerly flow on days when observational datasets indicate such flow directions offshore of CA. NAAPS is a global aerosol forecast model run by the U.S. Naval Research Laboratory (NRL) in Monterey, CA that predicts 3-dimensional anthropogenic and biogenic fine (ABF), dust, sea salt, and biomass burning smoke particle concentrations in the atmosphere. NAAPS relies on meteorological data derived from the Navy Global Environmental Model (NAVGEM; Hogan et al., 2014) and considers 25 vertical levels in the troposphere. For this study, we utilized the reanalysis version of NAAPS (NAAPS-RA, hereafter called NAAPS) that assimilates aerosol depth observations to get a general sense of the simulated differences between southerly and northerly flow days for our region of focus and as a complement to the aircraft data.

The motivation for the usage of these models is two-fold. The NAAPS-RA has a coarse horizontal resolution; however, it provides large-scale aerosol conditions with observational constraints on the model fields (i.e., incorporates satellite retrieved aerosol optical depth). It is important to have this relatively accurate large-scale aerosol background information for regional aerosol-cloud interaction research, as some of the background aerosol information (e.g., biomass burning smoke) and pollution are advected into the interested study area. Another minor reason is for model evaluation purposes: to see if models with different resolutions can resolve the studied phenomena, as this is less studied and is of interest to check if models have the capability to represent them. The use of NAAPS and COAMPS provides insight into how aerosol-cloud interactions from in situ data are represented by coarse resolution models.

We investigated data for northward wind speed (v_{wind}, where northward (i.e., southerly) flow is indicated by positive values) and mass concentrations for ABF aerosols and sea salt (Fig. 2), along with smoke, dust, coarse aerosol, and fine aerosol (Fig. S2). Note that ABF represents secondarily formed species (SO_4^{2-} and secondary organic aerosol) and primary organic aerosol generally within the fine mode (<1 µm). To be approximately similar to the average boundary layer height of all the missions used in this study, the first five vertical levels (max height of ~668 m above sea level) of NAAPS were used for data analysis. Vertical profiles of temperature for each campaign categorized by flow regime are provided in Fig. S3 using aircraft data over the ocean, to show the general structure of the lower troposphere in relation to the first five vertical levels of NAAPS.

For our analysis, the NAAPS data were first separated into southerly and northerly flow days for each campaign based on results from Sect. 2.2, and the average value of each parameter was calculated for four reported times: 0000, 0600, 1200, and 1800 UTC. The most focus is placed on 1800 UTC, as that time coincided with most Twin Otter flight periods (results for the remaining time periods are in Fig. S4-S10). Then, all the parameters except v_{wind} were summed across the five vertical levels to get a total mass concentration (µg m^{-3}) up to ~668 m above sea level, whereas the average was calculated for v_{wind}. Those values were used to calculate the difference between southerly and northerly flow days at $1.0° \times 1.0°$ spatial resolution.

COAMPS is a high-resolution meteorological forecast model developed by the NRL's Marine Meteorology Division (MMD) that outputs parameters like air temperature, winds, precipitation, cloud base and top heights, and mass concentrations for the same aerosol species as those in NAAPS. For this study, we assessed the wind speed/direction and smoke from COAMPS and NAAPS for the purpose of contrasting with observational data. COAMPS maps were generated for this study by NRL at three different resolutions: 45 km, 15 km, and 5 km. To compare to NAAPS, 15 km resolution grids were used. To assess the efficacy of COAMPS and NAAPS at forecasting heavy pollution on a day with southerly winds, we performed a comparison of the two models for CSM RF 6 at 1800 UTC to match the flight time. The focus areas for both COAMPS and NAAPS matched that of the aircraft data mentioned in Sect. 2.1.1. The altitudes used for the COAMPS maps for wind speed/direction and smoke were 762 m and 660 m, respectively, as the best match to the NAAPS maximum altitude used in this work.

2.4   IMPROVE

To investigate the difference in surface-level aerosol measurements between southerly and northerly flow days, this study utilized composition data from the Interagency Monitoring of Protected Visual Environments (IMPROVE) network (Malm et al., 1994; http://views.cira.colostate.edu/fed/). Data were taken from the Pt. Reyes

National Seashore surface station (38.07° N, 122.88° W) for the full campaign months shown in Table 1. Every third day, gravimetric mass of particulate matter ($PM_{2.5}$ and PM_{10}) was measured. The $PM_{2.5}$ fraction was further analyzed via ion chromatography and X-ray fluorescence (XRF) for water-soluble ions and elements, respectively, along with organic and elemental carbon (OC and EC).

This study specifically investigated ($\mu g\ m^{-3}$): $PM_{2.5}$, coarse mass ($PM_{coarse} = PM_{10} - PM_{2.5}$), Cl^-, NO_3^-, SO_4^{2-}, Ni, K^+, Si, V, EC, OC, and fine soil. The total OC measurement comes from a summation of four fractions of OC, which are categorized by a method of carbon analysis detection temperature (e.g., Chow et al., 1993; Watson et al., 1994). This method quantifies methane produced via volatilization of particulate species in pure helium at 120°C (OC1), 250°C (OC2), 450°C (OC3), and 550°C (OC4). Similarly, the total EC measurement is a summation of three fractions categorized via combustion temperatures in a 98% pure helium and 2% pure oxygen environment: 550°C (EC1), 700°C (EC2), and 800°C (EC3). Fine soil concentrations are calculated as follows (Malm et al., 1994):

$$Fine\ soil\ (\mu g\ m^{-3}) = 2.2 \times [Al] + 2.49 \times [Si] + 1.63 \times [Ca] + 2.42 \times [Fe] + 1.94 \times [Ti] \tag{2}$$

This equation was confirmed by several studies (e.g., Cahill et al., 1981; Pitchford et al., 1981; Malm et al., 1994) through comparisons of resuspended soils and ambient particles.

Upon examination, it was decided to only use data for E-PEACE and BOAS because those campaign periods had more than a single point with valid data for southerly days (three and two, respectively); recall that IMPROVE data are only available every third day due to the sample collection procedure, so some southerly days would not necessarily have available IMPROVE data. All the species analyzed had a status flag of "V0" ("Valid value") or "V6" ("Valid value but qualified due to non-standard sampling conditions"), which are both considered valid data. We chose to include data flagged as "V6" (Cl^-, NO_3^-, and SO_4^{2-} for BOAS) due to the small quantity of usable data for southerly days. Additional information, like sampling protocols, are provided elsewhere (http://vista.cira.colostate.edu/Improve/sops/). Like the aircraft and CW data, Mann-Whitney U tests were performed on this dataset to determine if the median species concentrations were equivalent for southerly and northerly days across a campaign.

2.5   MODIS

To assess cloud characteristics of southerly and northerly flow days during the campaign months of this study, we retrieved daily mean values within the same focus region defined for aircraft data in Sect. 2.1.1 (35.31° N – 40.99° N, 125.93° W – 118.98° W) for the following properties from the MODerate resolution Imaging Spectroradiometer (MODIS) on Aqua through NASA Giovanni (https://giovanni.gsfc.nasa.gov/giovanni/): cloud effective particle radius (r_e; µm), cloud liquid water path (LWP; $g\ m^{-2}$), cloud optical thickness (COT), cloud fraction (from cloud mask), and aerosol optical depth (AOD, combined dark target and deep blue at 0.55 µm for land and ocean). N_d (cm^{-3}) was calculated from MODIS properties based on the following equation (Painemal and Zuidema, 2011):

$$N_d = 1.4067 \times 10^{-6}[cm^{-0.5}] \times \frac{COT^{0.5}}{r_e^{2.5}} \tag{3}$$

Additionally, retrieval data were only used when cloud fraction ≥ 30% to maximize both data reliability and sample size (Mardi et al., 2021). The focus of the analysis is comparing median values of these remotely sensed variables between southerly and northerly days for E-PEACE and BOAS due to a similar LWP value for the two flow regimes (66.48/67.17 $g\ m^{-2}$ and 84.40/89.90 $g\ m^{-2}$, respectively). Data for the other campaigns are included in the SI. Additionally, this study used MODIS visible imagery on NASA Worldview to qualitatively identify smoke plumes, in addition to fire radiative power from the MODIS Fire Information for Resource Management System (FIRMS; https://earthdata.nasa.gov/firms).

3   Results and Discussion
3.1   Lower Tropospheric Wind Profile

We first examine NAAPS and airborne observations for the lower tropospheric wind profile during the periods of analysis shown in Table 1. Note that the other datasets described in Sect. 2.2 are consistent with the airborne wind results and thus only NAAPS and aircraft data are discussed here for two reasons: NAAPS results are used to assess how such a model quantifies differences in winds between southerly and northerly flow days as identified with

methods in Sect. 2.2, whereas aircraft data provide insight into typical wind speeds during southerly and northerly flow periods.

Beginning with the aircraft data, results are discussed here only for measurements over the ocean with the $N_{a>10nm}$ filter applied to remove smoke influence (Table 3). The mode of wind directions during southerly and northerly flow days in each campaign expectedly aligned with southerly (144° – 194°) and northerly flow (327° – 332°), respectively, because of how the classification was done (Sect. 2.2). Median wind speeds across each campaign ranged from 2.35 – 7.75 m s^{-1} for southerly flow in contrast to 5.12 – 8.87 m s^{-1} for northerly flow. This finding differs from what has been observed in previous studies, likely due to the difference in sampling location: aircraft observations from the surface to 800 m versus buoy/surface observations, respectively. All campaigns featured higher median wind speeds for northerly flow flights. However, when looking at the vertical wind profiles of each campaign for southerly and northerly flow days (Fig. S11), there were several instances where median wind speed at the surface for southerly flow days was greater than for northerly flow days. Both the median wind speeds and directions of southerly and northerly days were significantly distinct from one another for all of the studied campaigns (Table S4).

Table 3: Median values (southerly/northerly) of various parameters over the ocean with an $N_{a>10nm}$ filter such that RFs with median $N_{a>10nm} > 7,000$ cm^{-3} were removed from the final analysis to eliminate smoke interference. Mode values are used for wind direction. The instruments used for the parameters from left to right are as follows: CPC 3010, CPC 3010 – PCASP$_{<1μm}$, PCASP$_{<1μm}$, PCASP$_{>1μm}$, CPC 3025/CPC 3010, CASF. The far right-hand columns indicate the number of datapoints used from each campaign, with n_{Na} indicating the amount of data used for all N_a calculations, n_{Nd} is for cloud data, and n_{Wind} is for wind speed and direction. FSSP data were used for N_d data only during BOAS, whereas CASF was used in other campaigns. These data are for the lowest 800 m above sea level. The reader is referred to Fig. S12 for box plots corresponding to the analysis in this table, as well as Table S4 for Mann-Whitney U p-values.

	$N_{a>10nm}$ (cm^{-3})	$N_{a10-100nm}$ (cm^{-3})	$N_{a0.1-1μm}$ (cm^{-3})	$N_{a>1μm}$ (cm^{-3})	$N_{a3}:N_{a10}$ (-)	N_d (cm^{-3})	Wind Speed (m s^{-1})	Wind Direction (°)	n_{Na} (×10^3)	n_{Nd} (×10^3)	n_{Wind} (×10^3)
E-PEACE	861 / 703	501 / 454	338 / 197	0 / 1.25	1.09 / 1.10	252 / 163	3.38 / 7.58	177.61 / 330.48	20.3 / 202.7	17.1 / 127.1	37.4 / 330.8
NiCE	953 / 606	248 / 245	471 / 260	2.51 / 0	1.12 / 1.17	249 / 254	3.80 / 5.12	180.81 / 327.20	1.4 / 66.8	1.5 / 39.6	3.0 / 112.8
BOAS	750 / 497	553 / 256	204 / 196	0 / 1.24	1.20 / 1.18	143 / 127	5.49 / 6.35	166.97 / 328.58	5.8 / 72.1	3.9 / 20.5	11.8 / 104.7
FASE	836 / 916	423 / 635	326 / 180	0 / 0	1.29 / 1.16	203 / 223	2.35 / 6.82	144.03 / 331.29	1.0 / 95.5	0.3 / 99.2	1.3 / 194.9
MACAWS	722 / 815	560 / 635	154 / 164	0 / 0	1.25 / 1.26	189 / 165	7.75 / 8.87	162.15 / 330.28	10.3 / 118.9	6.6 / 27.0	16.9 / 145.9
CSM	5,558 / 3,451	5,081 / 3,366	515 / 365	1.00 / 0	1.30 / 1.67	334 / 314	6.10 / 6.77	193.93 / 332.16	4.8 / 31.5	1.8 / 4.1	6.9 / 41.3

For context, boundary layer flow patterns from NAVGEM are provided in Fig. S13 for all southerly and northerly days at 1800 UTC (Fig. S14 and S15 provide flow maps for each individual campaign). The average southerly flow pattern (Fig. S13a) captures generally weaker flow, particularly near Marina, CA, where a slight reversal can be observed. When looking at the flow maps for each campaign (Fig. S14 and S15), only BOAS and FASE captured a small wind reversal by Marina, CA during southerly flow days. Both MACAWS and CSM had a circulatory-pattern north of Marina, CA, near Pt. Reyes, and southerly flow is more clearly observed during the CSM campaign along the coast.

NAAPS values are discussed for v_{wind} for the lowest ~668 m above sea level, with positive (negative) values representing southerly (northerly) flow (Fig. 2). This altitude range coincides with the airborne data shown in Table 3. The v_{wind} data are categorized into "Southerly Days," "Northerly Days," and "Difference" (i.e., southerly – northerly values) for 1800 UTC, which overlaps with most of the Twin Otter flight times (Fig. 1); results for 0000, 0600 and 1200 UTC are provided in Fig. S4. Both southerly and northerly days had weaker v_{wind} closer to the coast (up to 35° N) compared to farther offshore over the ocean (~ -3/-9 and -4/-6 m s^{-1}, respectively, for southerly/northerly flow). Slow, slightly northerly winds extended farther north to Marina and west to 123.5° W for southerly days, which is illustrated in red (differences exceeding ~3 m s^{-1} between flow regimes) in the "Difference" panel. Northerly days also had an area of weaker v_{wind} north of 43.5° N, which is emphasized in the "Difference" panel in blue (differences of -4 – -6 m s^{-1}). NAAPS was not able to fully capture southerly winds over the ocean and along the coast in that v_{wind} was not clearly positive (i.e., not northward); however, the magnitude of the wind speed difference along the coastal area of the study domain appeared to align with the mechanics of coastal wind reversal and CTDs: the weakening of

399 northerly wind and ultimate reversal of flow (e.g., Winant et al., 1987; Melton et al., 2009). A key conclusion from
400 NAAPS is that the difference between southerly and northerly flow days matches expectations with southerly days
401 having a greater tendency towards higher v_{wind} compared to northerly days, but still not necessarily distinctly positive
402 v_{wind} values.
403
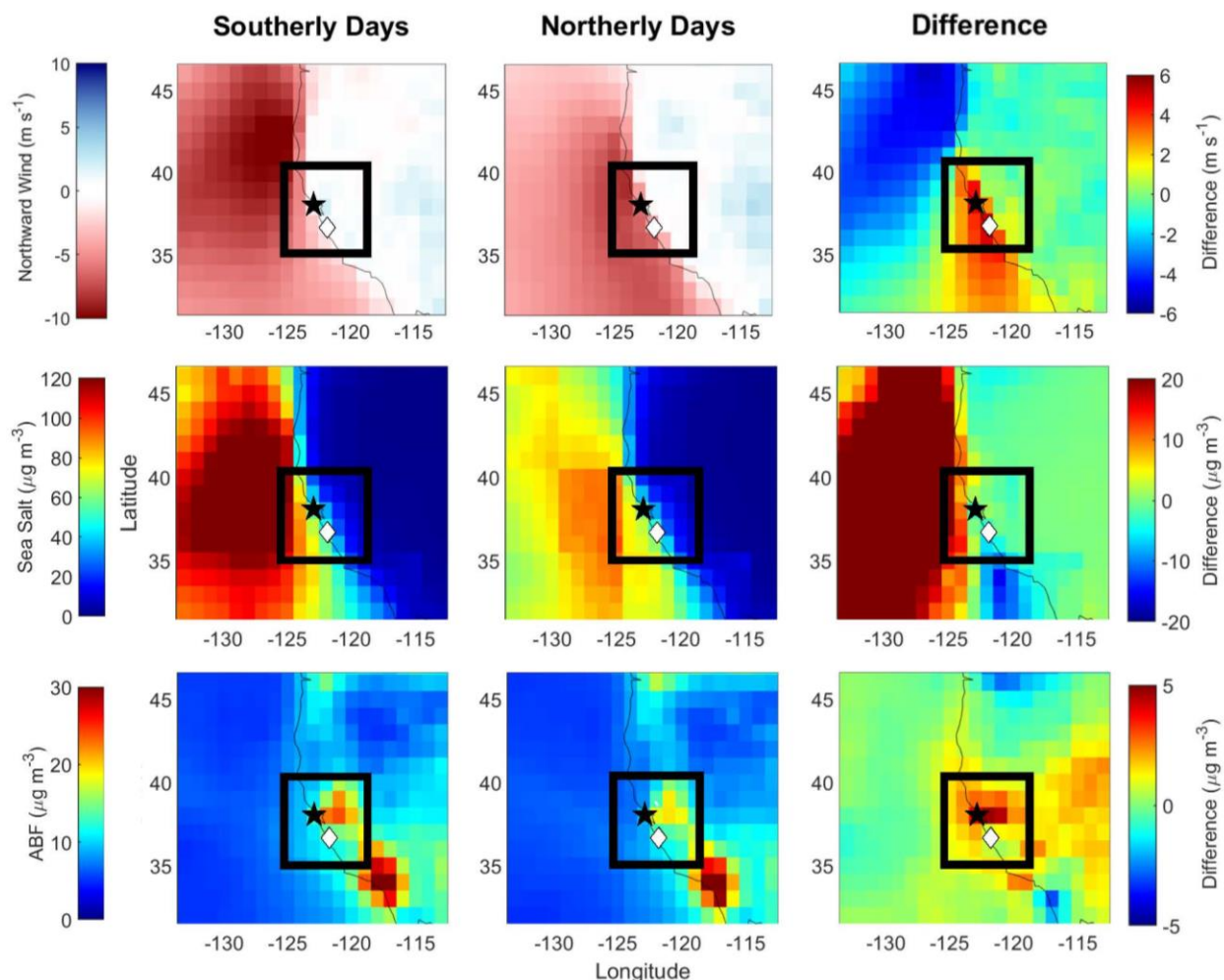
404
405 **Figure 2: Average northward wind speed (v_{wind}; m s^{-1}), total sea salt mass concentration (µg m^{-3}), and total ABF mass**
406 **concentration (µg m^{-3}) of campaign months at 1800 UTC for 1st through 5th NAAPS levels (up to ~668 m above sea level)**
407 **for southerly and northerly flow wind days. The right-most panel illustrates the difference between southerly and northerly**
408 **flow days. The airbase in Marina, CA is denoted by a white diamond, Pt. Reyes is indicated with a black star, and the black**
409 **box indicates the region of focus in this study.**
410
411 **3.2   Aerosol Response to Southerly Flow**
412 **3.2.1   Fire Radiative Power Maps**
413   Prior to discussing aerosol results, we address the influence of wildfire emissions, which is an aerosol
414 source that varies in terms of strength between the six campaign periods in contrast to shipping and other forms of
415 continental emissions that are more consistent year to year. Past studies using airborne and surface-based data at
416 Marina, CA (airbase indicated by a white diamond in Fig. 1 and 2) overlapping with the six campaigns in Table 1
417 revealed the following in terms of notable biomass burning influence around Marina and offshore areas (e.g.,
418 Prabhakar et al., 2014; Braun et al., 2017; Mardi et al., 2018): (i) E-PEACE/BOAS: no major influence of note; (ii)
419 NiCE: influence around the last week of July 2013; (iii) FASE: influence between 25 July and 12 August; (iv)
420 MACAWS: significant influence on flights during 28 June and 3 July owing to the aircraft having flown close to
421 wildfire areas inland in northern CA; (v) CSM: significant influence throughout the campaign. These archived notes

422 do not preclude the possibility of biomass burning influence during other periods of those campaigns as it relates to
423 Twin Otter aerosol and cloud measurements.
424   Spatial maps of fire radiative power (FRP; Fig. 3), indicative of burn intensity, show relatively less burning
425 activity in immediate proximity to Marina during E-PEACE and BOAS. In contrast, the other campaigns show
426 clusters of burning spots around Marina. Note that CSM, by virtue of its name, was focused largely on wildfires
427 with dedicated RFs to sample smoke. MACAWS also was designed as a wildfire study but had less cases of strong
428 plumes to sample, which included RFs on 28-29 June farther inland than most RFs, resulting in very high aerosol
429 number concentrations ($N_{a>10nm}$ > 10,000 cm^{-3}). These maps are mainly contextual to show the spatial distribution of
430 fire sources and specific conclusions cannot be gleaned solely based on these regarding which campaigns had more
431 or less wildfire influence overlapping with the flight tracks. This is especially the case because smoke can be
432 advected from far distances away from the study region. The wildfire filter described in Sect. 2.1 aims to filter out a
433 large portion of smoke influence, at least at the regional level.
434

435 **3.2.2   Fine Aerosol**
436   The first hypothesis of this study is that southerly flow yields higher fine aerosol levels associated with
437 anthropogenic and continental tracer species due to more perceived influence from land and shipping sources (Juliano
438 et al., 2019a; 2019b). This was also speculated by Hegg et al. (2008) although it was not examined in great detail by
439 that study. Here we rely on results from a number of datasets including measurements from the Twin Otter (Tables 3
440 and 4) and the Pt. Reyes IMPROVE site (Fig. 4), along with NAAPS model results (Fig. 2).
441

442 **3.2.2.1   Airborne: Particle Concentration**
443   Beginning with the Twin Otter data, aerosol data for 17 southerly flight days corresponding to 21 RFs were
444 compared to 93 other flight days with predominantly northerly flow in Table 3 (box plots of the variables are in Fig.
445 S12, and Mann-Whitney U test results are in Table S4), as well as Tables S1-S3. We focus primarily on flight data
446 over the ocean with the $N_{a>10nm}$ filter applied to omit wildfire influence; the other aircraft data result tables in the
447 Supplement generally show the same trends as Table 3. We caution that the results of FASE, and to a slightly lesser
448 extent NiCE, are not as meaningful as the other campaigns owing to the least amount of data for southerly conditions,
449 with numbers of datapoints shown in the tables.
450   The total submicron aerosol number concentration, $N_{a>10nm}$, was far larger for southerly flow (722-5,558 cm^{-3}
451) as compared to northerly flow flights (497-3,451 cm^{-3}). Of the six campaigns, the only ones with higher median
452 values in northerly flow were FASE and MACAWS, with small $\Delta N_{a>10nm}$ of -80 cm^{-3} and -93 cm^{-3}, respectively. CSM
453 exhibited the largest difference in median values for $N_{a>10nm}$ between southerly and northerly flow ($\Delta N_{a>10nm}$ = 2,107
454 cm^{-3}), followed by NiCE ($\Delta N_{a>10nm}$ = 347 cm^{-3}) and BOAS ($\Delta N_{a>10nm}$ = 253 cm^{-3}). While these campaigns have a
455 smaller relative sample size of southerly data ($n_{Na} < 6 \times 10^3$; CSM: 4.8×10^3, NiCE: 1.4×10^3; and BOAS: 5.8×10^3), E-
456 PEACE has a sizable amount of southerly data (20.3×10^3) and the least fire influence of the missions included in this
457 study, so we find it may be the most reliable campaign to analyze. There was a distinct difference between southerly
458 and northerly days during E-PEACE as well, with a $\Delta N_{a>10nm}$ of 158 cm^{-3}. As the number concentration in the
459 submicron range dominates the total CPC concentrations, these results convincingly point to an enhancement of fine
460 aerosol pollution in southerly flow even without the $N_{a>10nm}$ filter (Table S1).
461   We examined various size ranges of particles in the submicron range as well. For particles between 10-100
462 nm, southerly conditions generally had higher number concentrations except again for FASE and MACAWS and with
463 more comparable levels during NiCE. As particles larger than 100 nm are more relevant for cloud condensation nuclei
464 (CCN) activity, we also examined number concentrations for diameters between 0.1 and 1 µm, which show higher
465 southerly levels except for MACAWS. Between campaigns, CSM overall exhibited the highest particle concentrations
466 in this size range due to extensive wildfire emissions in the area, which are known to be linked with enhanced levels
467 of particles larger than 100 nm in the same region (Mardi et al., 2018), which is why this campaign shows relatively
468 large PCASP enhancements in both southerly and northerly flow conditions relative to the other campaigns (see in
469 particular Tables S1-S2). Without the CPC filter (Table S1), only the medians for NiCE and BOAS on northerly wind
470 days changed, resulting in the $N_{a10-100nm}$ median during NiCE to be lower during southerly flow days compared to
471 northerly days. When looking within the region of focus, the inclusion of land data in addition to ocean data (Tables
472 S2-S3) leads to significant N_a differences (to a lesser extent for the filtered data, Table S3) compared to Table 3,
473 including higher submicron concentrations for NiCE, BOAS, and FASE.
474
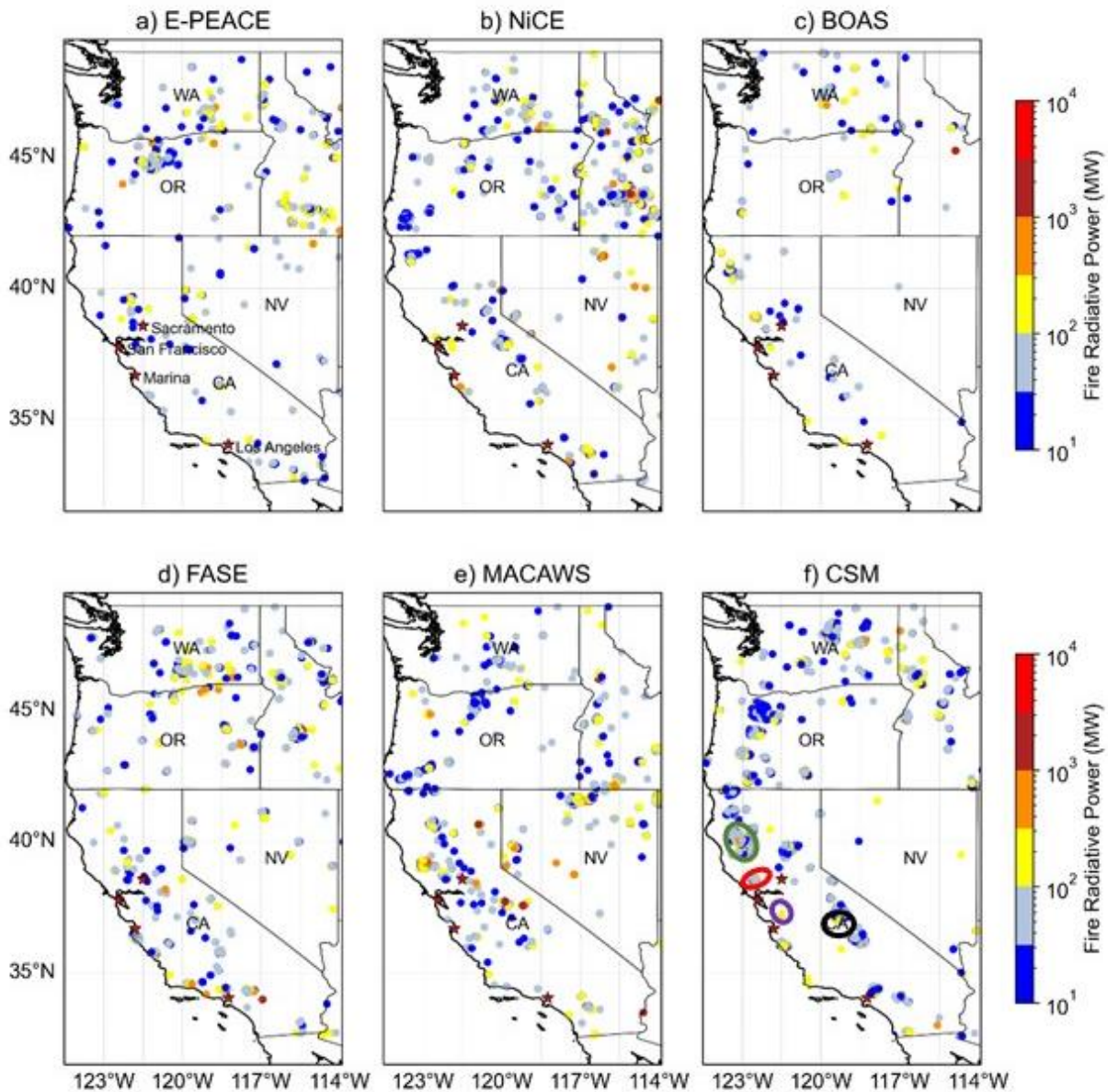
475
476 **Figure 3: Spatial maps of fire radiative power (FRP), downloaded from the MODIS Fire Information for Resource**
477 **Management System (FIRMS; https://earthdata.nasa.gov/firms) for the entire months spanning individual field**
478 **campaigns in Table 1. Only FRP values with a high detection confidence level (≥ 80%) are shown (Giglio et al., 2015). The**
479 **circled areas in panel (f) correspond to some of the largest wildfires in CA state history that occurred in 2020 that are**
480 **referred to in Sect. 3.4.2: August Complex fire (green), SCU Lightning Fire Complex (purple), Creek fire (black), and**
481 **LNU Lightning Complex fire (red).**

482
483   Although new particle formation (NPF) was not expected to be prominent in the lower 800 m owing mostly
484 to high aerosol surface areas especially due to sea spray emissions, we still examined the ratio of N_a above 3 nm
485 relative to 10 nm (N_{a3}:N_{a10}), as this ratio is a commonly used marker for identifying NPF. Such instances are more
486 common in the free troposphere in the study region owing to reduced aerosol surface areas (Dadashazar et al., 2019).
487 The results suggest that the N_{a3}:N_{a10} ratios for the two flow regimes were significantly different for all the campaigns
488 except for MACAWS (higher ratios in southerly flow for BOAS and FASE), with median flow direction-dependent

489 values per campaign ranging from 1.09 to 1.30. During CSM, the median ratio value was 1.67 in northerly flow
490 conditions due to presumed influence from high precursor levels in smoke plumes.
491
492 **3.2.2.2   Airborne: Tracer Species in Cloud Water**
493   We next turn to CW composition data (Table 4) to continue learning more about the effect of southerly flow
494 and its associated emission sources. NiCE and FASE were not included in the CW calculations of Table 4 (but shown
495 in Fig. S16) because there were fewer than five samples from RFs with southerly wind direction for those two
496 campaigns, and CW was not collected during CSM. NO_3^- and nss-SO_4^{2-}, both representative of fine aerosol pollution,
497 were higher for southerly days, with a significant difference (Table S5) apparent in E-PEACE (1.80/0.30 and 2.10/0.81
498 $\mu g\ m^{-3}$ for southerly and northerly days, respectively), as well as for NO_3^- during BOAS (1.02/0.23 $\mu g\ m^{-3}$ for southerly
499 and northerly days, respectively). The same trend was observed for V (ship exhaust tracer) and NH_4^+, which can be
500 used as a tracer for continental sources such as agriculture (Juliano et al., 2019b). Thus, these results help to provide
501 more confidence in results from Juliano et al. (2019b) but with increased sampling across more campaigns. For E-
502 PEACE and MACAWS, there were also lower southerly flow concentrations of K^+ (0.01/0.05 and 0.06/0.11 $\mu g\ m^{-3}$)
503 and Ca^{2+} (0.05/0.07 and 0.06/0.16 $\mu g\ m^{-3}$), suggestive of less influence from biomass burning and dust sources with
504 the caveat that K^+ and Ca^{2+} have sources other than biomass burning and dust.
505   There were also higher concentrations of oxalate during southerly days, which can be used as a tracer for
506 aqueous processing (Hilario et al., 2021), wherein cloud droplets are formed from oxidized volatile organic
507 compounds (Ervens et al., 2011; Ervens, 2015; Mcneill, 2015). Further, there were significant differences in median
508 concentrations between southerly and northerly flow days during BOAS and MACAWS (0.12/0.05 and 0.08/0.03 μg
509 m^{-3}, respectively). Precursors to oxalate are diverse including from biogenic sources, biomass burning, combustion
510 (e.g., Stahl et al., 2020 and references therein), shipping, along with being associated with sea salt and dust owing to
511 gas-particle partitioning (Sorooshian et al., 2013; Stahl et al., 2020; Hilario et al., 2021); such sources are presumed
512 to be influential during southerly flow based on the notion that air masses are influenced by some combination of
513 continental emissions and extended time in shipping lanes.
514   Cloud water pH was lower and thus more acidic on southerly days for all three campaigns (3.85/4.54,
515 4.30/4.34, 4.33/4.62 for southerly/northerly days during E-PEACE, BOAS, and MACAWS, respectively, and
516 statistically different for E-PEACE and BOAS), which is another indicator for anthropogenic pollution enriched with
517 acidic species (Pye et al., 2020). Increased acid levels can result in more Cl^- depletion when considering sea salt
518 particles (e.g., Edwards et al., 2023 and references therein); interestingly, southerly days were characterized by lower
519 Cl^-:Na^+ ratios with median values of 1.39 (MACAWS), 1.63 (E-PEACE) (both campaigns of which southerly days
520 were significantly different from northerly flow days), and 2.48 (BOAS), although the difference in MACAWS was
521 only 0.12. Braun et al. (2017) noted that, theoretically, over 60% of the Cl^- depletion in the submicron range could be
522 attributed to nss-SO_4^{2-}, and greater than 20% in the supermicron range could be attributed to NO_3^-. As was noted
523 previously, nss-SO_4^{2-} and NO_3^- were noticeably enhanced during southerly flow days while the Cl^-:Na^+ ratios were
524 reduced. Schlosser et al. (2017) also reported that organic acids, notably oxalate, were significantly enhanced during
525 periods of Cl^- depletion, which is reflected in our CW data. As E-PEACE was statistically the most robust dataset (and
526 all CW species except Ca^{2+}, NH_4^+, and oxalate had medians that were significantly different between southerly and
527 northerly flow days), the results from CW convincingly align with more shipping and/or continental influence in
528 southerly flow to impact cloud composition.
529
530 **Table 4: Median values (southerly/northerly) of water-soluble CW composition ($\mu g\ m^{-3}$) over the entirety of three**
531 **campaigns with sufficient data. The starred (*) values are reported in ng m^{-3}. The number of samples used in each campaign**
532 **is in the far-right hand column (n). The reader is referred to Table S5 which shows the p-values from the Mann-Whitney**
533 **U tests, as well as Fig. S16 which shows box plots of the CW composition results for the five campaigns with available data.**
534 **Values shown as "–" denote when samples were below the limit of detection.**

	Ca^{2+}	Cl^-/Na^+	K^+	Na^+	NH_4^+	NO_3^-	Oxalate	pH	nss-SO_4^{2-}	V	n
E-PEACE	0.05 / 0.07	1.63 / 2.15	0.01 / 0.05	0.42 / 1.21	— / —	1.80 / 0.30	0.02 / 0.02	3.85 / 4.54	2.10 / 0.81	2.16* / 0.38*	10 / 65
BOAS	0.11 / 0.08	2.48 / 2.74	0.06 / 0.06	1.99 / 1.55	0.44 / 0.04	1.02 / 0.23	0.12 / 0.05	4.30 / 4.34	1.08 / 0.83	— / 0.15*	5 / 21

MACAWS	0.06 / 0.16	1.39 / 1.51	0.06 / 0.11	1.30 / 2.70	0.08 / 0.05	0.55 / 0.38	0.08 / 0.03	4.33 / 4.62	0.56 / 0.26	0.07* / 0.05*	15 / 51

3.2.2.3   Surface: Aerosol Composition

We next examine surface composition data from the Pt. Reyes IMPROVE site. Mass concentrations of twelve PM composition variables were investigated to analyze important tracers along the coast (Fig. 4), with Mann-Whitney U test p-values for comparing southerly and northerly flow days shown in Table S6. It is important to recall that E-PEACE and BOAS were the only campaigns that had more than a single day of valid data coinciding with southerly flow because of the added challenge of IMPROVE sampling occurring every third day; therefore, northerly days had significantly more data points (18 for E-PEACE and seven for BOAS) compared to southerly days (three and two, respectively). That is the general reason for the large whiskers on the box plots for northerly RFs during E-PEACE and the lack of whiskers for southerly RFs during BOAS. Another feature to note is the 'folded over' appearance of some of the box plots. This indicates a high variance within the dataset and a skewed distribution. We caution that this analysis is not very statistically robust owing to the rare nature of southerly days in overlap with IMPROVE sampling; however, we take a 'better than nothing' approach to use in a supportive role in comparison to other datasets used to assess differences between southerly and northerly flow.
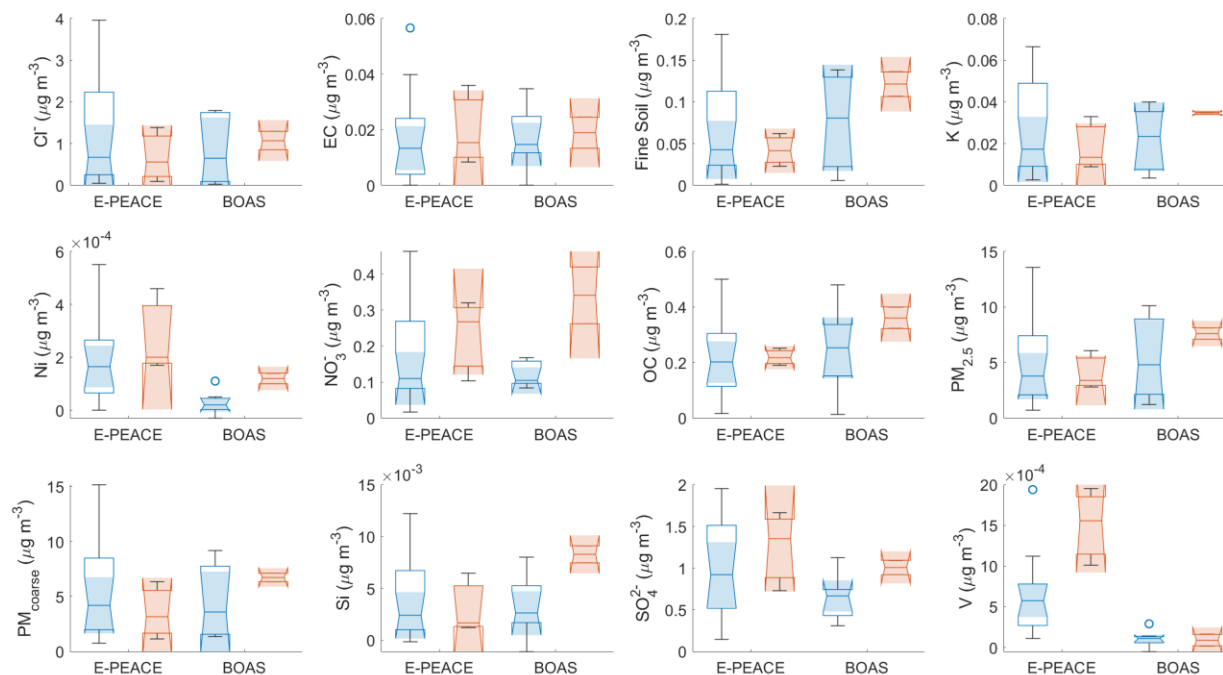
Figure 4: Box plots of IMPROVE data from the Pt. Reyes surface station. The southerly data for E-PEACE and BOAS (three and two points, respectively) are represented by the red boxes, and the northerly data (18 and seven, respectively) are represented by the blue boxes.

SO_4^{2-}, NO_3^-, OC, V, Ni, and EC are reasonable tracer species representative of either shipping and/or continental sources in the study region, as they have been utilized as tracers for these sources in previous studies (Wang et al., 2014; Maudlin et al., 2015; Wang et al., 2016; Dadashazar et al., 2019; Ma et al., 2019). These species were hypothesized to be more enhanced in the coastal CA zone on southerly flow days due to air spending time over shipping lanes and land upwind of the study region. Even with the limited southerly flow sample data, the results of Fig. 4 support this idea as southerly conditions coincide with higher median concentrations of these species than northerly days. The most striking relative differences were for NO_3^- (southerly/northerly): 0.27/0.11 and 0.34/0.10 µg m^{-3} for E-PEACE and BOAS, respectively. NO_3^- was the only species during BOAS that was found to have a median

563 concentration that was statistically different between southerly and northerly days (Table S6). Ni and V are the primary
564 trace metals in heavy ship fuel oils and are commonly used as tracers for ship emissions (Celo et al., 2015; Corbin et
565 al., 2018), and V was previously found enhanced in CW linked to ship emissions in E-PEACE (Coggon et al., 2012;
566 Prabhakar et al., 2014). There were mostly higher concentrations of these species on southerly flow days (E-PEACE
567 southerly/northerly: 0.20/0.17 and 1.56/0.58 ng m^{-3}, respectively; BOAS southerly/northerly: 0.12/0.02 and 0.09/0.11
568 ng m^{-3}, respectively), supporting the hypothesis of elevated shipping emissions. Also, a Mann-Whitney U test found
569 that the median V concentrations during E-PEACE were statistically different for southerly and northerly days (Table
570 S6).
571   Only BOAS exhibited higher PM$_{2.5}$ during southerly days compared to northerly days (7.61/4.82 µg m^{-3},
572 respectively), with E-PEACE having roughly equivalent concentrations for the two flow regimes (3.39/3.78 µg m^{-3},
573 respectively). This is likely owing to how PM$_{2.5}$ is not the best marker for shipping and continental emissions owing
574 to its inclusion of other species of marine and natural origin.
575
576 **3.2.2.4   NAAPS: Aerosol Composition**
577   To round out discussion of fine aerosol pollution, we discuss NAAPS model results (Fig. 2). The largest
578 enhancements in ABF mass concentrations occurred inland both north of Marina around Pt. Reyes and near the Ports
579 of Los Angeles and Long Beach. There was >5 µg m^{-3} difference in ABF concentration between southerly and
580 northerly days near Pt. Reyes. This suggests that while there were elevated levels of anthropogenic emissions in this
581 area regardless of the flow regime, there were increased concentrations during southerly flow days according to
582 NAAPS. An example HYSPLIT back-trajectory for a southerly flow day (Fig. S17) shows air masses with likely
583 influence from as far south as southern California and the U.S.-Mexico border. Additionally, there is a strong ABF
584 signal (>30 µg m^{-3}) around 34° N, 118° W for both categories of days, which is close to the Ports of Los Angeles and
585 Long Beach, two of the busiest container ports (in terms of cargo volume processed) in the United States and areas
586 with elevated levels of NO$_x$ and SO$_x$ due to the ship exhaust and port emissions (Corbett and Fischbeck, 1997). As
587 can be seen in the Fig. S6, the ABF concentrations around 34° N, 118° W and 38° N, 122° W increase throughout the
588 day, with more significant increases north of the ports for southerly flow days. On southerly flow days, NAAPS results
589 point to marked enhancements in fine aerosol and smoke mass concentration north of Pt. Reyes over water but with
590 mostly a reduction in such values to the south of Pt. Reyes over water. ABF represents the category of species that are
591 most tied to the tracer species shown already to be enhanced in southerly flow, and thus at least this result from
592 NAAPS is consistent with enhanced values across most of the study domain in southerly flow.
593
594 **3.2.3   Supermicron Aerosol**
595   While this study hypothesizes that most of the aerosol changes in southerly flow will pertain to submicron
596 aerosol, we still discuss supermicron aerosol characteristics to determine if there was any change observed. With all
597 the complexities leading to sea salt emissions in the region (Schlosser et al., 2020), which is the predominant
598 supermicron aerosol type in the study region's boundary layer, combined with the shifting wind directions and speeds
599 leading up to and after a wind reversal (e.g., Juliano et al., 2019a), there was no underlying expectation for a change
600 in levels during southerly flow events. Beginning with the aircraft observations, N$_{a>1µm}$ levels were generally low and
601 usually zero in terms of flight median values simply due to so many zero values during a RF. Northerly flow conditions
602 yielded median levels exceeding zero for E-PEACE (1.25 cm^{-3}) and BOAS (1.24 cm^{-3}). In contrast, southerly flow led
603 to levels of 2.51 cm^{-3} and 1.00 cm^{-3} during NiCE and CSM, respectively. The enhancement during southerly flow
604 during at least CSM is presumed to be due to pervasive smoke during many of those RFs. However, the small median
605 concentrations for each campaign make it hard to definitively determine if the lower concentrations during E-PEACE
606 and BOAS were due to changes in flow regime or another factor. Figure S1 shows a scatterplot of total CASF number
607 concentration versus effective diameter to separate out where cloud droplets are relative to probable sea salt particles
608 and then coarse aerosol associated with the wildfires. There is considerable data coverage at LWC < 0.02 g m^{-3}, with
609 effective diameters below 5 µm and number concentrations exceeding 10 cm^{-3}, with the latter surpassing what would
610 be expected from sea salt (e.g., Gonzalez et al., 2022). It is very likely that dust particles can be entrained into regional
611 smoke plumes as discussed in past work for the region (e.g., Maudlin et al., 2015; Schlosser et al., 2017). This will be
612 discussed in more detail for a case flight demonstrating such high levels during southerly flow in Sect. 3.4.2.
613   Airborne CW results reveal generally no strong trends in either sea salt or dust tracer species between the
614 flow regimes. The sea salt tracer species Na$^+$ was lower for southerly days during E-PEACE (and statistically different)

and MACAWS (0.42/1.21 and 1.30/2.70 µg m^{-3} for southerly/northerly days) but with an increase during BOAS (1.99 versus 1.55 µg m^{-3}). The dust tracer species Ca^{2+} was, expectedly, much less abundant compared to Na$^+$, without significant differences between flow regimes. However, as already noted (Sect. 3.2.2.2), the fine pollution in southerly flow likely still influenced supermicron aerosol characteristics via Cl$^-$ depletion in salt particles.

In terms of IMPROVE data, PM$_{coarse}$, Si, fine soil, and Cl$^-$ are the variables that would best coincide with typical sources of supermicron aerosol (i.e., dust and sea salt). They did not reveal any consistent trend for the two campaigns. Based on the lack of a general trend and reduced data for southerly flow days, it is concluded that there is insufficient evidence from IMPROVE to conclude that there is more or less dust or salt influence on southerly days.

The wind profile discussed in Sect. 3.1 has implications for sea salt aerosol production, which is influenced by wind speed. The breaking of wave crests to produce (mostly coarse mode) spray droplets occurs at strong wind conditions (>10 m s^{-1}) (Monahan et al., 1986). Additionally, jet droplets are produced via bubble bursting at lower wind speeds (>5 m s^{-1}; Blanchard and Woodcock, 1957; Fitzgerald, 1991; Wu, 1992; Moorthy and Satheesh, 2000). On southerly days, there were faster northerly winds over the open ocean offshore west of 125° W, which corresponded to high sea salt concentrations (>100 µg m^{-3}) according to NAAPS, whereas northerly days had slower v_{wind} and less sea salt (65 – 90 µg m^{-3}) in those same areas farther offshore. In contrast, in the coastal areas south of 35° N, northerly days had higher sea salt concentrations (by 10 – 20 µg m^{-3}) than southerly days with weaker (less negative) v_{wind}. NAAPS shows the same general trends for coarse aerosol mass compared to sea salt, with dust being far less abundant and more spatially heterogeneous in terms of enhancements and reductions between southerly and northerly conditions. In general, the NAAPS results are consistent with aircraft and IMPROVE results in that in the study domain, there was not any pronounced difference in coarse aerosol characteristics during southerly flow. More research and data would be helpful, though, to put this conclusion on firmer ground.

3.3   Cloud Responses
3.3.1   Airborne In Situ Results

As most campaigns exhibited higher N_a on southerly flight days, it matches expectation that most campaigns exhibited higher N_d values for southerly days (southerly/northerly values): E-PEACE (252/163 cm^{-3}), BOAS (143/127 cm^{-3}), MACAWS (189/165 cm^{-3}), and CSM (334/314 cm^{-3}). These campaigns had southerly N_d values that were ~ 20$\pm$4 cm^{-3} greater than the median values on northerly days, with a significant difference during E-PEACE (ΔN_d ~ 89 cm^{-3}). E-PEACE also had the most cloud data points compared to the other missions, qualifying it as the most robust campaign for inspection of cloud properties. The remaining two campaigns had the least amount of cloud data during southerly flow conditions (NiCE and FASE) and thus those results are of less importance to discuss. CSM had the highest N_d concentrations for both southerly and northerly days due to the strongest levels of pollution (from smoke) relative to the other campaigns.

3.3.2   Satellite Data Results

The second part of our hypothesis was that there would be a noticeable difference in cloud properties like N_d, r_e, and COT between southerly and northerly flow days (at fixed LWP), namely due to the change in emissions sources. In particular, we anticipated higher N_d and COT and lower r_e for southerly flow periods due to the Twomey effect (Twomey, 1974) and higher particle concentrations from continental pollution and shipping emissions. Six parameters were retrieved from MODIS, divided into southerly and northerly days for E-PEACE and BOAS, and visualized as box plots (Fig. 5). Cloud LWP medians for southerly and northerly days within E-PEACE (66.48/67.17 g m^{-2}) and BOAS (84.40/89.90 g m^{-2}) were not significantly different. Therefore, these two campaigns are the focus here, unlike the other campaigns that had larger differences (Table S7). The medians for N_d were higher for southerly days (138.54/91.99 cm^{-3} and 96.59/72.80 cm^{-3} for southerly/northerly wind days during E-PEACE and BOAS, respectively), and the southerly and northerly medians during E-PEACE were significantly different from one another. Consistent with the Twomey effect (Twomey, 1974), the median r_e for southerly flow days was lower than northerly flow days (9.94/11.97 µm and 11.77/13.29 µm), with the medians during E-PEACE being significantly different. Cloud optical thickness was also higher for southerly days compared to northerly days for both campaigns (10.27/8.42 and 11.88/10.87 for E-PEACE and BOAS, respectively); however, the medians for each flow regime were not found to be significantly different from one another. We note that even NiCE with LWP values being slightly higher for southerly days (82.78 g m^{-2} versus 74.54 g m^{-2}), the same general results are observed with southerly days having

666 higher N_d/COT and reduced r_e (Table S7); the other three campaigns did not follow these N_d/COT/r_e trends due to the
667 larger LWP differences between flow regimes.
668   Although no differences were necessarily expected, we still examined cloud fraction and AOD, which were
669 similar within a campaign for the two types of days (0.47/0.44 versus 0.58/0.57, and 0.10/0.09 versus 0.12/0.11,
670 respectively, for southerly and northerly wind days during E-PEACE versus BOAS). Based on these results, N_d, r_e,
671 and COT differences between flow regimes match our hypothesis, and two out of the three parameters during E-
672 PEACE were found to be significantly different between southerly and northerly days.
673
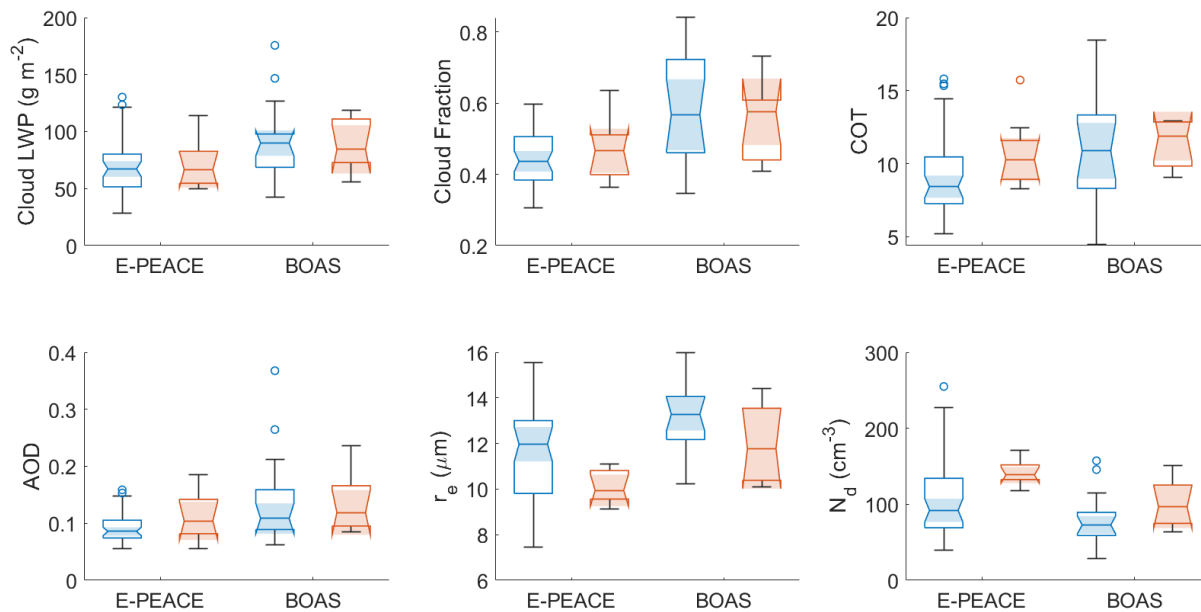
674
675 **Figure 5: Box plots of MODIS data within the study region during the periods overlapping with E-PEACE and BOAS. The**
676 **southerly data for E-PEACE and BOAS (eight points each) are represented by the red boxes, and the northerly data (44**
677 **and 17 points, respectively) are represented by the blue boxes. The notches (and shading, which helps to more clearly**
678 **indicate where the notches end) of the boxes assist in the determination of significance between multiple medians. If the**
679 **notches overlap, the medians are not significantly different from one another.**
680
681 **3.4   Case Studies**
682   In addition to looking at whole campaigns, we also looked closely at two RFs with southerly wind direction:
683 NiCE RF 16 (29 July 2013) and CSM RF 6 (10 September 2020). NiCE RF 16 was a unique flight, which coincided
684 with a CTD event (Bond et al., 1996; Nuss, 2007) and its flight path extended past 125° W into a large stratocumulus
685 cloud clearing (Crosbie et al., 2016; Dadashazar et al., 2020), which was unusual for the Twin Otter flights. CSM RF
686 6 was on a heavily polluted day owing to biomass burning emissions during one of the worst wildfire periods in CA
687 history. These case studies help emphasize the complexity of flow patterns in the region that influence the ability of
688 aerosols from different sources to arrive at the boundary layer in the study region. The observed changes in aerosol
689 and cloud properties between northerly and southerly days are likely not due to an instant switch in flow direction but
690 rather there is critical nuance in the timing, strength, and duration of the wind reversal, along with likely influence
691 from free tropospheric aerosol which can be sourced from various continental areas across California and even farther
692 away (Dadashazar et al., 2019).
693
694 **3.4.1   NiCE Research Flight 16**
695   NiCE RF 16 (29 July 2013) occurred on a day with a large stratocumulus cloud deck clearing, which, at its
696 widest point, was 150 km (Crosbie et al., 2016). As noted in Crosbie et al. (2016), this was a CTD event during the
697 time of the flight, and the boundary layer wind reversal (and resulting northwesterly flow) occurred under the

698 stratocumulus cloud deck within 100 km of the coast (~ 36.7° N, 123° W). The location of the wind reversal was
699 known, which allowed us to investigate if there was any apparent gradient in aerosol and cloud variables from the
700 coast to out over the ocean. The aircraft departed from Marina at approximately 1700 UTC, with a nearly straight,
701 westward path (Fig. 6a) toward the clear-cloudy boundary (reader is referred to Fig. 1a of Crosbie et al., 2016 for
702 boundary location). At the clear-cloudy interface (~ 36.7° N, 125° W, 1845 – 2000 UTC), stacked legs were performed
703 at multiple levels in both the MBL and FT on both sides of the boundary. Subsequently, the aircraft returned to Marina
704 following the initial outbound path. To visualize the location and general timing of the wind reversal (Fig. 6b-c), 48-
705 hr back-trajectories from HYSPLIT were used. This contrasts with the 24-hr back trajectories used to confirm
706 southerly wind flow in Sect. 2.2. For the case studies, 48-hr periods were used to have a better understanding of air
707 mass history. This case of southerly wind is one where the sampled air mass was likely to have spent more time in the
708 coastal area just south of Marina as compared to traditional northerly flow, where there was presumed influence from
709 shipping emissions and possibly advected continental air.
710
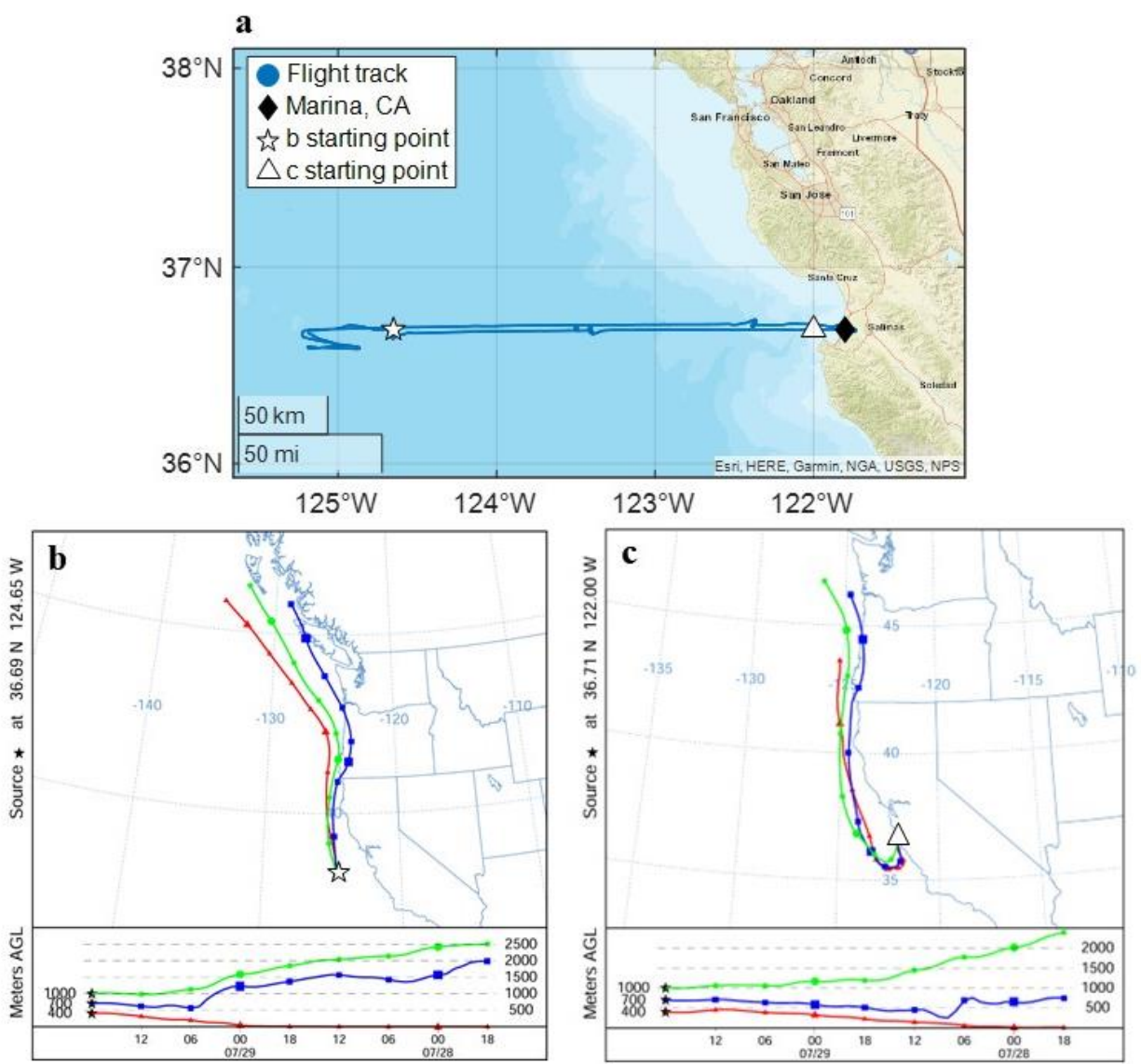
711
712 **Figure 6: (a) NiCE RF 16 (07/29/2013) flight track, with Marina represented by a solid black diamond, the starting point**
713 **of the HYSPLIT back-trajectory in panel (b) indicated by a white star, and the starting point of the HYSPLIT back-**
714 **trajectory in panel (c) indicated by a white triangle. (b) 48-hour back trajectory of a point (36.69° N, 124.65° W) along the**

719 We investigated gradients from the coast to farther offshore including past the wind reversal for several
720 parameters, including N_a, N_d, and AMS total mass and mass fractions, both in the sub-cloud MBL (<525 m AGL, Fig.
721 7) and in the FT (>765 m AGL, Fig. S18), both altitudes of which were defined in Crosbie et al. (2016). There was a
722 general trend of decreasing number concentration, especially for $N_{a0.1-1\mu m}$, $N_{a>10nm}$, and N_d, from the coast to slightly
723 before the stacked legs at the far west point (1,245/189, 1,240/390, and 772/263 cm^{-3}, respectively, at ~1732/1830
724 UTC). There was a wide range of supermicron concentrations for the whole flight duration, however, generally, there
725 was a slight decrease of $N_{a>1\mu m}$ along the flight path going west as well, but it was not as pronounced as the other
726 variables (24/4 cm^{-3}).
727 The eastbound leg to Marina was an interesting situation as there was no longer southerly flow closer to the
728 coast yet there was still a concentration increase for number and cloud drop concentrations but not up to the same
729 maximum levels that were observed on the westbound portion of the flight, probably owing to the reduced influence
730 from areas south of the sampling area ($N_{a0.1-1\mu m}$: 248/435, $N_{a>10nm}$: 454/752, N_d: 272/434, and $N_{a>1\mu m}$: 5/19 cm^{-3}, for
731 eastbound/westbound legs at ~2000/2037 UTC). AMS mass concentrations dropped significantly in the outbound
732 portion of the flight, from total mass as high as 10.16 µg m^{-3} (~1730 UTC) to 1.55 µg m^{-3} (~1745 UTC), the latter of
733 which was approximately 10 km offshore. During that period, organic mass fraction decreased from 0.81 to 0.28 in
734 favor of growing SO_4^{2-} mass fraction from 0.11 to 0.50. On the inbound track, similar to N_a/N_d results, there was not
735 as much of an enhancement in total mass (max of 4.41 µg m^{-3} at ~2040 UTC) and the chemical profile revealed more
736 comparable levels of SO_4^{2-} and organic mass fractions (0.39 and 0.52, respectively, at ~2040 UTC) in contrast to the
737 outbound track that showed higher organic mass fraction right by the coast.
738 The results suggest that the enhanced residence time of air masses (due to the wind reversal) in an area with
739 presumed influence from shipping emissions (see Fig. 9 in Coggon et al., 2012) and continental pollution yielded an
740 offshore gradient in N_a, N_d, and aerosol composition. Also, the results help show that this general coastal zone area in
741 the location of the wind reversal is enhanced with fine pollution, which generally will affect aerosol and cloud
742 characteristics if air masses spend prolonged time in it during southerly flow conditions. This all being said, it is hard
743 to unambiguously attribute the aerosol and cloud changes to emissions from a particular area and source due to the
744 complex flow nature in both the horizontal and vertical directions during the wind reversal period. This case study
745 helps motivate continued research studying these events.
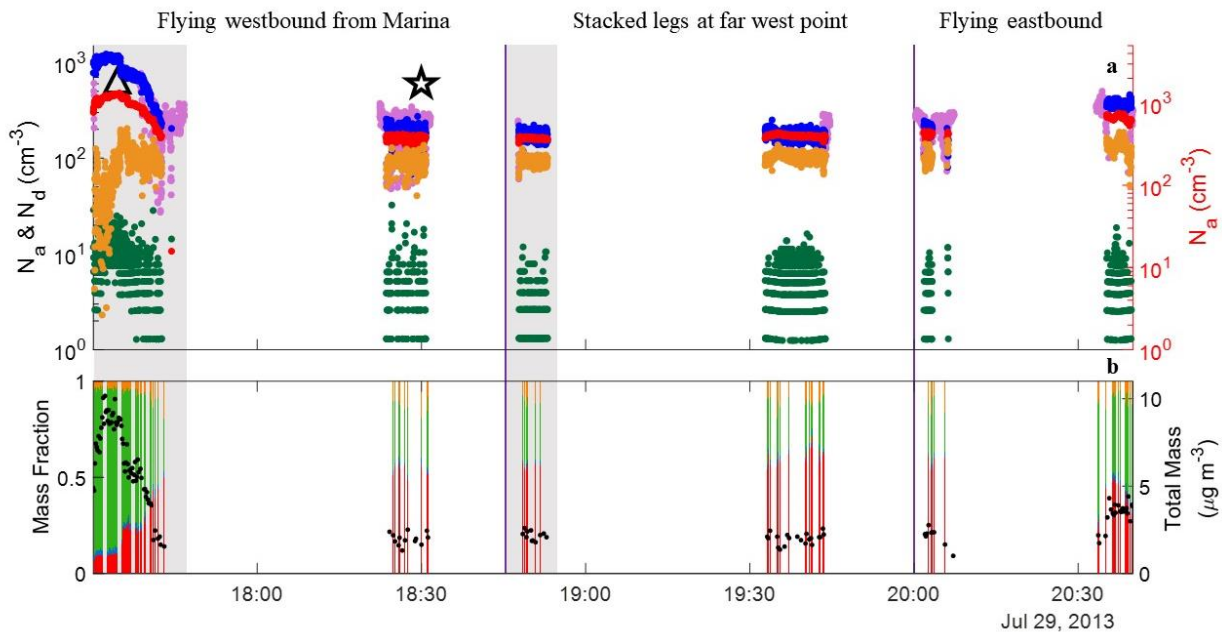
Figure 7: Data from NiCE RF 16 in the MBL (<525 m). The grey shading indicates time periods with mostly southerly winds, and the purple lines across all graphs indicate flight zones (outbound track, stacked legs at farthest west point, and inbound track). (a) The colored points on the left-hand axis correspond to $N_{a0.1-1\mu m}$ (blue, PCASP$_{<1\mu m}$), $N_{a>1\mu m}$ (green, PCASP$_{>1\mu m}$), and N_d (light purple, CASF). The colored points on the right-hand axis correspond to $N_{a>10nm}$ (red, CPC) and $N_{a10-100nm}$ (yellow, CPC 3010 – PCASP$_{<1\mu m}$). The triangle corresponds to the HYSPLIT back-trajectory end point seen in Fig. 6c, and the star corresponds to the HYSPLIT back-trajectory end point seen in Fig. 6b. (b) Stacked bar plot of AMS mass fractions of SO_4^{2-} (red), NO_3^- (blue), organics (green), and NH_4^+ (orange), overlayed with total mass concentration (μg m^{-3}; black).

The trends in the FT are much more ambiguous than those in the MBL (Fig. S18). Similar to the MBL, there was a decrease in $N_{a0.1-1\mu m}$ and $N_{a>10nm}$ from the coast to near the stacked legs (2,467/395 and 2,820/689 cm^{-3}, respectively, at ~1726/1844 UTC), however there was no discernable trend for $N_{a>1\mu m}$. There were no apparent offshore trends for AMS total mass or speciated mass fractions. Additionally, on the eastbound flight leg, there was not a clear trend for any of the parameters. This suggests that the effects of the southerly winds were stronger in the MBL than the FT.

3.4.2   CSM Research Flight 6

CSM stands out among all of the examined campaigns owing to the strength and temporal persistence of wildfire plumes, which was also the main focus of the mission. Of the top 3% (n = 12) of the largest fires in CA in the historical record, four occurred in 2020 (circled in Fig. 3): the August Complex fire (16 August, Mendocino County), the SCU Lightning Fire Complex (18 August, Santa Clara County), the Creek fire (4 September, Madera County), and the LNU Lightning Complex fire (16 August, Hapa County) (Keeley and Syphard, 2021). These four fires were a mix of both merged (August Complex) and unmerged (LNU Lightning Complex) fires that burned over 417, 160, 153, and 146 kha, respectively, and burned for months after they were ignited.

CSM RF 6 (10 September 2020) included two major components (Fig. 8a): a spiral over Salinas (max altitude of 6,172 m at ~2000 UTC) and a spiral over Monterey Bay (max altitude of 4,822 m at ~ 2170 UTC). The entire region was heavily impacted by smoke during CSM RF 6 (Fig. 8b). Additionally, around 36.5° N, 125° W, there is an area not dominated by smoke, but rather, clouds, pointing to the likelihood of smoke-cloud interactions in the region on not just this day but other CSM days with similar smoky conditions. HYSPLIT back-trajectories for the two spirals for a 48-hr period were generated (Fig. 8c and 8d). For the spiral over Monterey Bay (Fig. 8c), the lowest altitude trajectory (trajectory beginning at 400 m) is mostly northwesterly, the second lowest altitude (trajectory beginning at 1400 m) is primarily southerly, and the highest altitude (trajectory beginning at 2400 m) is approximately northeasterly. The highest altitude back-trajectory passes over the LNU Lightning Complex fire (red oval; circled in Fig. 3). For the spiral over Salinas (Fig. 8d), all three altitude levels (400, 800, and 1200 m AGL) reveal southerly trajectory paths, and the air masses from the second-highest altitude back-trajectory possibly had some influence from the SCU Lightning Fire Complex (purple oval) and the August Complex Fire (green oval) due to offshore and northerly flow in the preceding 36-hr (Fig. 3).
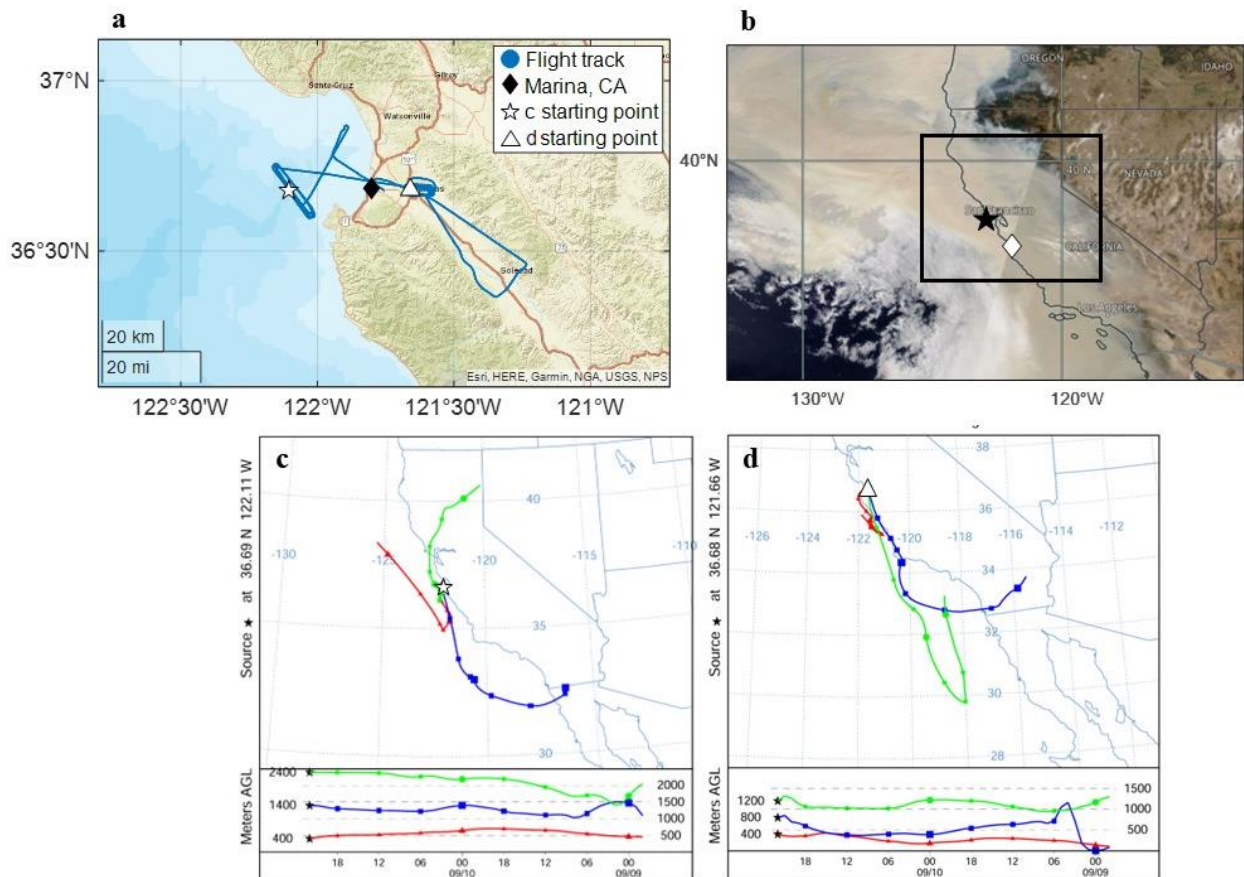
786
787 **Figure 8: (a) CSM RF 6 (09/10/2020) flight track, with Marina, CA represented by a solid black diamond, the starting point**
788 **of the HYSPLIT back-trajectory in panel (c) indicated by a white star, and the starting point of the HYSPLIT back-**
789 **trajectory in panel (d) indicated by a white triangle. (b) NASA Worldview image, with Marina, CA represented by a white**
790 **diamond, and Pt. Reyes denoted by a black star. (c) 48-hour back trajectory of a point (36.69° N, 122.11° W) along the flight**
791 **path during the sounding over Monterey Bay (HYSPLIT end time: 2100 UTC) at three different altitudes: 400, 1400, and**
792 **2400 m. (b) 48-hour back trajectory of a point (36.68° N, 121.66° W) along the flight path during the sounding over Salinas**
793 **(HYSPLIT end time: 1900 UTC) at three different altitudes: 400, 800, and 1200 m. (c) and (d) utilized different altitudes**
794 **for the back-trajectories to reflect the different maximum altitudes of the two major soundings of the flight.**

795

796   The vertical profiles of temperature, wind speed, and wind direction are provided in Fig. S19 for context.
797 Notably, the vertical region with southerly flow was thicker over the ocean (approximately 370 – 3700 m) versus over
798 land (540 – 2900 m). N_a for different size ranges and $N_{a3}:N_{a10}$ are shown separately for land and over the ocean (Fig.
799 9). There was more variability in $N_{a>10nm}$ (Fig. 9a) over the ocean, with a general decrease in concentration with
800 increase in altitude for both data over land and ocean, followed by increasing $N_{a>10nm}$ above the region of primarily
801 southerly flow (non-shaded points). As illustrated by the composite boundary layer flow pattern in Fig. S15e-f, smoke
802 along the coast during southerly flow periods was re-circulated northwest of Marina, CA nearby the flight path (which
803 was not observed for the northerly composite flow pattern), which could have also influenced the elevated aerosol
804 concentrations during this flight. There was not much change in $N_{a>1\mu m}$ (medians = 1 – 3 cm^{-3}; range = 0 – 6 cm^{-3}; Fig.
805 9c) until >2.5 km, where concentration increases over land (medians = 5 – 97 cm^{-3}; range = 0 – 297 cm^{-3}) where there
806 is primarily northerly flow, likely from sampling smoke plumes. Over the ocean, low supermicron particle
807 concentrations are observed ($\leq$ 7 cm^{-3}). These results show that during extensive smoky periods, the flow regime does
808 not matter in cases like RF6 due to smoke generally being all across the region. Furthermore, the results show that
809 supermicron particle concentrations are certainly enhanced in smoke plumes, as has been observed before in the study
810 region (Mardi et al., 2018) but not to this pronounced extent, especially at high altitudes over land.

811   The $N_{a3}:N_{a10}$ ratio (Fig. 9d) was generally consistent over land across all vertical levels, with a good number
812   of outliers in the region of primarily southerly flow. The medians of the ratios over the ocean were usually lower than
813   the medians over land until 3.5 km. There was no discernable difference in the $N_{a3}:N_{a10}$ ratio over land between
814   southerly and northerly flow (medians approximately 1.35 until >5.5 km) or over the ocean (medians for both flow
815   regimes approximately 1.20, with a slight bump to 1.26 and 2.14 between 3.5 and 4.5 km). The reader is referred to
816   Sect. S1 (Supplement) for discussion about NAAPS and COAMPS results for this case study as they relate to flow
817   behavior and aerosol characteristics.
818
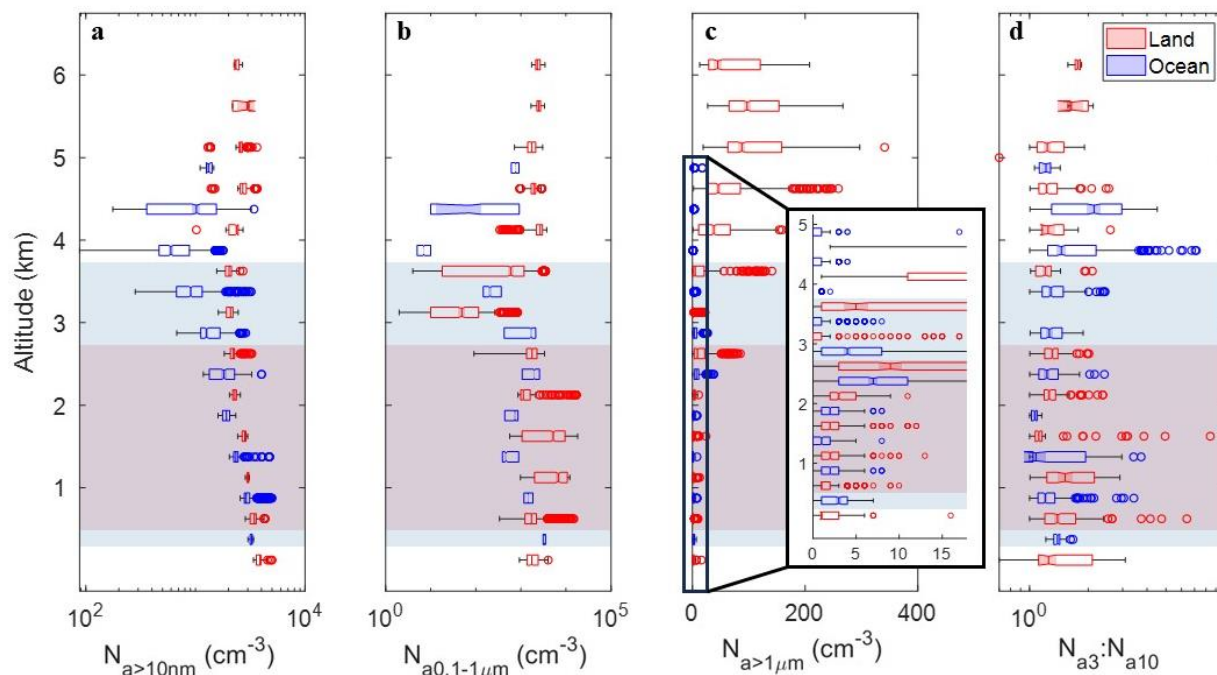
819
820   **Figure 9: CSM RF 6 box plot vertical profiles of (a) $N_{a>10nm}$ (cm^{-3}), (b) $N_{a0.1-1\mu m}$ (cm^{-3}; PCASP$_{<1\mu m}$), (c) $N_{a>1\mu m}$ (cm^{-3};**
821   **PCASP$_{>1\mu m}$), and (d) $N_{a3}:N_{a10}$. Data are shown every 500 m over land (red) and ocean (blue) above the MBL, which is the**
822   **maximum altitude of the first bins for all the panels. Panel (c) has an additional focus on altitudes ≤5 km ($N_{a>1\mu m}$ ≤ 18 cm^{-}**
823   **^{3}). The red and blue shading indicates altitudes over the land and ocean, respectively, with southerly winds.**

824
825   **4   Conclusions**

826   In this study, we utilized multiple types of data, including a large repository of NPS Twin Otter data, to
827   compare coastal aerosol and cloud characteristics near central CA for northerly and southerly wind regimes in the
828   lower troposphere. Juliano et al. (2019a) had previously called for future studies to utilize in situ observations to
829   support their investigation into cloud properties using satellite observations. Our study is among the first to investigate
830   aerosol and cloud droplet number concentrations through in situ aircraft data in addition to CW composition, and
831   intercompare those results with satellite data, as well as models and surface station data. This builds upon previous
832   studies, such as Juliano et al. (2019b), by utilizing similar data sources in greater proportions.
833   Our first hypothesis is proven correct in that more fine aerosol pollution is present off the CA coast during
834   southerly flow due to likely influence from shipping exhaust and continental emissions. We caution that there is
835   considerable complexity in flow patterns both horizontally and vertically when northerly winds change to southerly
836   winds and this warrants more research to study for instance how influential free tropospheric air is for the boundary
837   layer aerosol changes occurring on southerly flow days. Submicron aerosol pollution is found to be higher during
838   southerly flow days (particularly during E-PEACE), with respect to both N_a ($N_{a>10nm}$, $N_{a10-100nm}$, $N_{a0.1-1\mu m}$) and
839   concentrations of shipping and continental tracer species in surface data (SO$_4^{2-}$, NO$_3^-$, OC, V, Ni, and EC) and CW
840   samples (nss-SO$_4^{2-}$, NO$_3^-$, NH$_4^+$, V and oxalate). Cloud water is shown to be more acidic during southerly flow along
841   with more Cl$^-$ depletion based on lower Cl$^-$:Na$^+$ ratios. A secondary hypothesis was that increased influence from

842 shipping and/or continental emissions would lead to enhanced N_d and COT and lower r_e (at fixed LWP) due to the
843 Twomey effect (Twomey, 1974). Both the airborne in situ data and satellite retrievals show increased N_d on southerly
844 days. The satellite retrieval data also reveal higher COT and lower r_e during southerly flow The increase in N_d and
845 decrease in r_e associated with the northerly to southerly reversal matches results of a previous study in the region
846 (Juliano et al., 2019a). The analysis of CSM RF 6 reveals that during heavy biomass burning periods with prevailing
847 smoke, there is relatively no difference in aerosol or cloud properties associated with changes in flow regime. Based
848 on the NAAPS evaluation, while coarse-gridded models can capture differences in wind direction and aerosol
849 concentration between southerly and northerly flow days, they are not fully able to reproduce southerly flow.
850 A limitation in this type of study to address in the future is the difficulty of obtaining detailed in situ data
851 during southerly wind conditions. As noted already, wind reversals along coasts extend to a number of other global
852 regions (e.g., South America, southern Africa, Australia) and thus it is recommended to continue increasing the sample
853 data volume to better understand changes in aerosol and cloud properties as a function of wind direction along coastal
854 regions. Intercomparisons with models, as partly done here, can aid with determining if model resolution should
855 improve to better simulate these events. Generally speaking, the prevalence of fine aerosol on southerly flow days and
856 associated changes in cloud microphysical properties are important findings with implications for weather, health,
857 coastal ecology, and aviation.
858

Data availability

860 Airborne data used in this work can be accessed at https://doi.org/10.6084/m9.figshare.5099983.v11 (Sorooshian et
861 al., 2017). Buoy data from the NOAA's NDBC can be accessed at https://www.ndbc.noaa.gov/. The archived data
862 from GOES-West Full Disk Cloud Product (GOES-15) can be accessed at https://satcorps.larc.nasa.gov/. The archived
863 surface weather plots from NOAA's WPC can be accessed at
864 https://www.wpc.ncep.noaa.gov/archives/web_pages/sfc/sfc_archive.php. The surface data from IMPROVE can be
865 accessed at http://views.cira.colostate.edu/fed/. The MODIS-Aqua data can be accessed through NASA Giovanni at
866 https://giovanni.gsfc.nasa.gov/giovanni/. The FIRMS data can be accessed at https://earthdata.nasa.gov/firms.

Author contributions

868 AW and PX aided with access and interpretation of COAMPS and NAAPS data, respectively. KZ and GB conducted
869 the data analysis. KZ and AS conducted data interpretation. KZ and AS prepared the manuscript. All authors edited
870 the manuscript.

Competing interests

872 At least one of the (co-)authors is a member of the editorial board of Atmospheric Chemistry and Physics.

Disclaimer

874 Publisher's note: Copernicus Publications remains neutral with regard to jurisdictional claims in published maps and
875 institutional affiliations.
876

Acknowledgements

878 The authors acknowledge NPS staff for successfully conducting Twin Otter flights and all others who were involved
879 in the airborne campaigns. We thank Ewan Crosbie for useful discussions about this work.

880   **Financial support**

881   This work was funded by Office of Naval Research grant N00014-21-1-2115.
882
883

884   **References**
885

886   AzadiAghdam, M., Braun, R. A., Edwards, E.-L., Bañaga, P. A., Cruz, M. T., Betito, G., Cambaliza, M. O.,
887   Dadashazar, H., Lorenzo, G. R., Ma, L., MacDonald, A. B., Nguyen, P., Simpas, J. B., Stahl, C., and
888   Sorooshian, A.: On the nature of sea salt aerosol at a coastal megacity: Insights from Manila, Philippines in
889   Southeast Asia, Atmospheric Environment, 216, 116922, https://doi.org/10.1016/j.atmosenv.2019.116922, 2019.

890   Blanchard, D. C. and Woodcock, A. H.: Bubble formation and modification in the sea and its meteorological
891   significance, Tellus, 9, 145-158, 10.3402/tellusa.v9i2.9094, 1957.

892   Bond, N. A., Mass, C. F., and Overland, J. E.: Coastally trapped wind reversals along the United States west coast
893   during the warm season. Part I: Climatology and temporal evolution, Monthly Weather Review, 124, 430-445,
894   https://doi.org/10.1175/1520-0493(1996)124<0430:CTWRAT>2.0.CO;2, 1996.

895   Braun, R. A., Dadashazar, H., MacDonald, A. B., Aldhaif, A. M., Maudlin, L. C., Crosbie, E., Aghdam, M. A.,
896   Hossein Mardi, A., and Sorooshian, A.: Impact of wildfire emissions on chloride and bromide depletion in
897   marine aerosol particles, Environmental Science & Technology, 51, 9013-9021,
898   https://doi.org/10.1021/acs.est.7b02039, 2017.

899   Cahill, T. A., Ashbaugh, L. L., Eldred, R. A., Feeney, P. J., Kusko, B. H., and Flocchini, R. G.: Comparisons between
900   size-segregated resuspended soil samples and ambient aerosols in the western United States, in: Atmospheric
901   Aerosol, ACS Symposium Series, 167, American Chemical Society, 269-285, https://doi.org/10.1021/bk-1981-
902   0167.ch015, 1981.

903   Celo, V., Dabek-Zlotorzynska, E., and McCurdy, M.: Chemical characterization of exhaust emissions from selected
904   Canadian marine vessels: The case of trace metals and lanthanoids, Environmental Science & Technology, 49,
905   5220-5226, https://doi.org/10.1021/acs.est.5b00127, 2015.

906   Chow, J. C., Watson, J. G., Pritchett, L. C., Pierson, W. R., Frazier, C. A., and Purcell, R. G.: The dri thermal/optical
907   reflectance carbon analysis system: description, evaluation and applications in U.S. Air quality studies,
908   Atmospheric Environment. Part A. General Topics, 27, 1185-1201, https://doi.org/10.1016/0960-
909   1686(93)90245-T, 1993.

910   Coggon, M. M., Sorooshian, A., Wang, Z., Metcalf, A. R., Frossard, A. A., Lin, J. J., Craven, J. S., Nenes, A.,
911   Jonsson, H. H., Russell, L. M., Flagan, R. C., and Seinfeld, J. H.: Ship impacts on the marine atmosphere:
912   insights into the contribution of shipping emissions to the properties of marine aerosol and clouds, Atmospheric
913   Chemistry and Physics, 12, 8439-8458, https://doi.org/10.5194/acp-12-8439-2012, 2012.

914   Coggon, M. M., Sorooshian, A., Wang, Z., Craven, J. S., Metcalf, A. R., Lin, J. J., Nenes, A., Jonsson, H. H., Flagan,
915   R. C., and Seinfeld, J. H.: Observations of continental biogenic impacts on marine aerosol and clouds off the
916   coast of California, Journal of Geophysical Research: Atmospheres, 119, 6724-6748,
917   https://doi.org/10.1002/2013jd021228, 2014.

918   Corbett, J. J. and Fischbeck, P.: Emissions from ships, Science, 278, 823-824,
919   https://doi.org/10.1126/science.278.5339.823, 1997.

920   Corbin, J. C., Mensah, A. A., Pieber, S. M., Orasche, J., Michalke, B., Zanatta, M., Czech, H., Massabò, D., Buatier
921   de Mongeot, F., Mennucci, C., El Haddad, I., Kumar, N. K., Stengel, B., Huang, Y., Zimmermann, R., Prévôt, A.
922   S. H., and Gysel, M.: Trace metals in soot and PM2.5 from heavy-fuel-oil combustion in a marine engine,
923   Environmental Science & Technology, 52, 6714-6722, https://doi.org/10.1021/acs.est.8b01764, 2018.

924 Crosbie, E., Wang, Z., Sorooshian, A., Chuang, P. Y., Craven, J. S., Coggon, M. M., Brunke, M., Zeng, X., Jonsson,
925 H., Woods, R. K., Flagan, R. C., and Seinfeld, J. H.: Stratocumulus cloud clearings and notable thermodynamic
926 and aerosol contrasts across the clear–cloudy interface, Journal of the Atmospheric Sciences, 73, 1083-1099,
927 https://doi.org/10.1175/JAS-D-15-0137.1, 2016.

928 Dadashazar, H., Ma, L., and Sorooshian, A.: Sources of pollution and interrelationships between aerosol and
929 precipitation chemistry at a central California site, Science of The Total Environment, 651, 1776-1787,
930 https://doi.org/10.1016/j.scitotenv.2018.10.086, 2019.

931 Dadashazar, H., Crosbie, E., Majdi, M. S., Panahi, M., Moghaddam, M. A., Behrangi, A., Brunke, M., Zeng, X.,
932 Jonsson, H. H., and Sorooshian, A.: Stratocumulus cloud clearings: statistics from satellites, reanalysis models,
933 and airborne measurements, Atmospheric Chemistry and Physics, 20, 4637-4665, https://doi.org/10.5194/acp-
934 20-4637-2020, 2020.

935 Dorman, C. E.: Evidence of Kelvin waves in California's marine layer and related eddy generation, Monthly
936 Weather Review, 113, 827-839, https://doi.org/10.1175/1520-0493(1985)113<0827:EOKWIC>2.0.CO;2, 1985.

937 Edwards, E. L., Choi, Y., Crosbie, E. C., DiGangi, J. P., Diskin, G. S., Robinson, C. E., Shook, M. A., Winstead, E.
938 L., Ziemba, L. D., and Sorooshian, A.: Sea salt reactivity over the northwest Atlantic: An in-depth look using
939 the airborne ACTIVATE dataset, EGUsphere, 2023, 1-56, https://doi.org/10.5194/egusphere-2023-2575, 2023.

940 Ervens, B., Turpin, B. J., and Weber, R. J.: Secondary organic aerosol formation in cloud droplets and aqueous
941 particles (aqSOA): a review of laboratory, field and model studies, Atmospheric Chemistry and Physics, 11,
942 11069-11102, https://doi.org/10.5194/acp-11-11069-2011, 2011.

943 Ervens, B.: Modeling the processing of aerosol and trace gases in clouds and fogs, Chemical Reviews, 115, 4157-
944 4198, https://doi.org/10.1021/cr5005887, 2015.

945 Fitzgerald, J. W.: Marine aerosols: A review, Atmospheric Environment. Part A. General Topics, 25, 533-545,
946 https://doi.org/10.1016/0960-1686(91)90050-H, 1991.

947 Garreaud, R., Rutllant, J., and Fuenzalida, H.: Coastal lows along the subtropical west coast of South America:
948 Mean structure and evolution, Monthly Weather Review, 130, 75-88, https://doi.org/10.1175/1520-
949 0493(2002)130<0075:CLATSW>2.0.CO;2, 2002.

950 Garreaud, R. and Rutllant, J.: Coastal lows along the subtropical west coast of South America: Numerical simulation
951 of a typical case, Monthly Weather Review, 131, 891-908, https://doi.org/10.1175/1520-
952 0493(2003)131<0891:CLATSW>2.0.CO;2, 2003.

953 Giglio, L., Schroeder, W., Hall, J. V., and Justice, C. O.: Modis collection 6 active fire product user's guide revision
954 A, Department of Geographical Sciences. University of Maryland, 9, 2015.

955 Gill, A. E.: Coastally trapped waves in the atmosphere, Quarterly Journal of the Royal Meteorological Society, 103,
956 431-440, https://doi.org/10.1002/qj.49710343704, 1977.

957 Gonzalez, M. E., Corral, A. F., Crosbie, E., Dadashazar, H., Diskin, G. S., Edwards, E.-L., Kirschler, S., Moore, R.
958 H., Robinson, C. E., Schlosser, J. S., Shook, M., Stahl, C., Thornhill, K. L., Voigt, C., Winstead, E., Ziemba, L.
959 D., and Sorooshian, A.: Relationships between supermicrometer particle concentrations and cloud water sea salt
960 and dust concentrations: analysis of MONARC and ACTIVATE data, Environmental Science: Atmospheres, 2,
961 738-752, https://doi.org/10.1039/d2ea00049k, 2022.

962 Guan, S., Jackson, P. L., and Reason, C. J. C.: Numerical modeling of a coastal trapped disturbance. Part I:
963 Comparison with observations, Monthly Weather Review, 126, 972-990, https://doi.org/10.1175/1520-
964 0493(1998)126<0972:NMOACT>2.0.CO;2, 1998.

Hegg, D. A., Covert, D. S., and Jonsson, H. H.: Measurements of size-resolved hygroscopicity in the California coastal zone, Atmospheric Chemistry and Physics, 8, 7193-7203, https://doi.org/10.5194/acp-8-7193-2008, 2008.

Hilario, M. R. A., Crosbie, E., Bañaga, P. A., Betito, G., Braun, R. A., Cambaliza, M. O., Corral, A. F., Cruz, M. T., Dibb, J. E., Lorenzo, G. R., MacDonald, A. B., Robinson, C. E., Shook, M. A., Simpas, J. B., Stahl, C., Winstead, E., Ziemba, L. D., and Sorooshian, A.: Particulate oxalate-to-sulfate ratio as an aqueous processing marker: Similarity across field campaigns and limitations, Geophysical Research Letters, 48, https://doi.org/10.1029/2021gl096520, 2021.

Hodur, R. M.: The Naval Research Laboratory's Coupled Ocean/Atmosphere Mesoscale Prediction System (COAMPS), Monthly Weather Review, 125, 1414-1430, https://doi.org/10.1175/1520-0493(1997)125<1414:TNRLSC>2.0.CO;2, 1997.

Hogan, T., Liu, M., Ridout, J., Peng, M., Whitcomb, T., Ruston, B., Reynolds, C., Eckermann, S., Moskaitis, J., Baker, N., McCormack, J., Viner, K., McLay, J., Flatau, M., Xu, L., Chen, C., and Chang, S.: The Navy Global Environmental Model, Oceanography, 27, 116-125, https://doi.org/10.5670/oceanog.2014.73, 2014.

Holland, G. J. and Leslie, L. M.: Ducted coastal ridging over S.E. Australia, Quarterly Journal of the Royal Meteorological Society, 112, 731-748, https://doi.org/10.1002/qj.49711247310, 1986.

Juliano, T. W., Lebo, Z. J., Thompson, G., and Rahn, D. A.: A new perspective on coastally trapped disturbances using data from the satellite era, Bulletin of the American Meteorological Society, 100, 631-651, https://doi.org/10.1175/bams-d-18-0002.1, 2019a.

Juliano, T. W., Coggon, M. M., Thompson, G., Rahn, D. A., Seinfeld, J. H., Sorooshian, A., and Lebo, Z. J.: Marine boundary layer clouds associated with coastally trapped disturbances: Observations and model simulations, Journal of the Atmospheric Sciences, 76, 2963-2993, https://doi.org/10.1175/jas-d-18-0317.1, 2019b.

Juliano, T. W. and Lebo, Z. J.: Linking large-scale circulation patterns to low-cloud properties, Atmospheric Chemistry and Physics, 20, 7125–7138, https://doi.org/10.5194/acp-20-7125-2020, 2020.

Keeley, J. E. and Syphard, A. D.: Large California wildfires: 2020 fires in historical context, Fire Ecology, 17, https://doi.org/10.1186/s42408-021-00110-7, 2021.

Lynch, P., Reid, J. S., Westphal, D. L., Zhang, J., Hogan, T. F., Hyer, E. J., Curtis, C. A., Hegg, D. A., Shi, Y., Campbell, J. R., Rubin, J. I., Sessions, W. R., Turk, F. J., and Walker, A. L.: An 11-year global gridded aerosol optical thickness reanalysis (v1.0) for atmospheric and climate sciences, Geoscientific Model Development, 9, 1489-1522, https://doi.org/10.5194/gmd-9-1489-2016, 2016.

Ma, L., Dadashazar, H., Braun, R. A., MacDonald, A. B., Aghdam, M. A., Maudlin, L. C., and Sorooshian, A.: Size-resolved characteristics of water-soluble particulate elements in a coastal area: Source identification, influence of wildfires, and diurnal variability, Atmospheric Environment, 206, 72-84, https://doi.org/10.1016/j.atmosenv.2019.02.045, 2019.

MacDonald, A. B., Dadashazar, H., Chuang, P. Y., Crosbie, E., Wang, H., Wang, Z., Jonsson, H. H., Flagan, R. C., Seinfeld, J. H., and Sorooshian, A.: Characteristic vertical profiles of cloud water composition in marine stratocumulus clouds and relationships with precipitation, Journal of Geophysical Research: Atmospheres, 123, 3704-3723, https://doi.org/10.1002/2017jd027900, 2018.

Malm, W. C., Sisler, J. F., Huffman, D., Eldred, R. A., and Cahill, T. A.: Spatial and seasonal trends in particle concentration and optical extinction in the United States, Journal of Geophysical Research: Atmospheres, 99, 1347-1370, https://doi.org/10.1029/93JD02916, 1994.

Mardi, A. H., Dadashazar, H., MacDonald, A. B., Braun, R. A., Crosbie, E., Xian, P., Thorsen, T. J., Coggon, M. M., Fenn, M. A., Ferrare, R. A., Hair, J. W., Woods, R. K., Jonsson, H. H., Flagan, R. C., Seinfeld, J. H., and

1008   Sorooshian, A.: Biomass burning plumes in the vicinity of the California coast: Airborne characterization of
1009   physicochemical properties, heating rates, and spatiotemporal features, Journal of Geophysical Research:
1010   Atmospheres, 123, https://doi.org/10.1029/2018jd029134, 2018.

1011   Mardi, A. H., Dadashazar, H., Painemal, D., Shingler, T., Seaman, S. T., Fenn, M. A., Hostetler, C. A., and
1012   Sorooshian, A.: Biomass burning over the United States east coast and western North Atlantic Ocean:
1013   Implications for clouds and air quality, Journal of Geophysical Research: Atmospheres, 126,
1014   https://doi.org/10.1029/2021jd034916, 2021.

1015   Mass, C. F. and Albright, M. D.: Coastal Southerlies and Alongshore Surges of the West Coast of North America:
1016   Evidence of mesoscale topographically trapped response to synoptic forcing, Monthly Weather Review, 115,
1017   1707-1738, https://doi.org/10.1175/1520-0493(1987)115<1707:CSAASO>2.0.CO;2, 1987.

1018   Mass, C. F. and Steenburgh, W. J.: An observational and numerical study of an orographically trapped wind reversal
1019   along the west coast of the United States, Monthly Weather Review, 128, 2363-2397,
1020   https://doi.org/10.1175/1520-0493(2000)128<2363:AOANSO>2.0.CO;2, 2000.

1021   Maudlin, L. C., Wang, Z., Jonsson, H. H., and Sorooshian, A.: Impact of wildfires on size-resolved aerosol
1022   composition at a coastal California site, Atmospheric Environment, 119, 59-68,
1023   https://doi.org/10.1016/j.atmosenv.2015.08.039, 2015.

1024   McNeill, V. F.: Aqueous Organic Chemistry in the Atmosphere: Sources and chemical processing of organic
1025   aerosols, Environmental Science & Technology, 49, 1237-1244, https://doi.org/10.1021/es5043707, 2015.

1026   Melton, C., Washburn, L., and Gotschalk, C.: Wind relaxations and poleward flow events in a coastal upwelling
1027   system on the central California coast, Journal of Geophysical Research: Oceans, 114,
1028   https://doi.org/10.1029/2009jc005397, 2009.

1029   Monahan, E. C., Spiel, D. E., and Davidson, K. L.: A model of marine aerosol generation via whitecaps and wave
1030   disruption, in: Oceanic Whitecaps: And Their Role in Air-Sea Exchange Processes, edited by: Monahan, E. C.,
1031   and Niocaill, G. M., Springer Netherlands, Dordrecht, 167-174, https://doi.org/10.1007/978-94-009-4668-2_16,
1032   1986.

1033   Moorthy, K. K. and Satheesh, S. K.: Characteristics of aerosols over a remote island, Minicoy in the Arabian Sea:
1034   Optical properties and retrieved size characteristics, Quarterly Journal of the Royal Meteorological Society, 126,
1035   81-109, https://doi.org/10.1002/qj.49712656205, 2000.

1036   National Resource Council: Coastal meteorology: A review of the state of the science, Washington, D.C., 99,
1037   https://doi.org/10.17226/1991, 1992.

1038   Nuss, W. A., Bane, J. M., Thompson, W. T., Holt, T., Dorman, C. E., Ralph, F. M., Rotunno, R., Klemp, J. B.,
1039   Skamarock, W. C., Samelson, R. M., Rogerson, A. M., Reason, C., and Jackson, P.: Coastally trapped wind
1040   reversals: Progress toward understanding, Bulletin of the American Meteorological Society, 81, 719-744,
1041   https://doi.org/10.1175/1520-0477(2000)081<0719:CTWRPT>2.3.CO;2, 2000.

1042   Nuss, W. A.: Synoptic-scale structure and the character of coastally trapped wind reversals, Monthly Weather
1043   Review, 135, 60-81, https://doi.org/10.1175/MWR3267.1, 2007.

1044   Painemal, D. and Zuidema, P.: Assessment of MODIS cloud effective radius and optical thickness retrievals over the
1045   Southeast Pacific with VOCALS-REx in situ measurements, Journal of Geophysical Research: Atmospheres,
1046   116, n/a-n/a, https://doi.org/10.1029/2011jd016155, 2011.

1047   Parish, T. R.: Forcing of the summertime low-level jet along the California coast, Journal of Applied Meteorology,
1048   39, 2421-2433, https://doi.org/10.1175/1520-0450(2000)039<2421:FOTSLL>2.0.CO;2, 2000.

1049 Pitchford, M., Flocchini, R. G., Draftz, R. G., Cahill, T. A., Ashbaugh, L. L., and Eldred, R. A.: Silicon in submicron
1050   particles in the southwest, Atmospheric Environment (1967), 15, 321-333, https://doi.org/10.1016/0004-
1051   6981(81)90035-4, 1981.

1052 Prabhakar, G., Ervens, B., Wang, Z., Maudlin, L. C., Coggon, M. M., Jonsson, H. H., Seinfeld, J. H., and
1053   Sorooshian, A.: Sources of nitrate in stratocumulus cloud water: Airborne measurements during the 2011 E-
1054   PEACE and 2013 NiCE studies, Atmospheric Environment, 97, 166-173,
1055   https://doi.org/10.1016/j.atmosenv.2014.08.019, 2014.

1056 Pye, H. O. T., Nenes, A., Alexander, B., Ault, A. P., Barth, M. C., Clegg, S. L., Collett Jr, J. L., Fahey, K. M.,
1057   Hennigan, C. J., Herrmann, H., Kanakidou, M., Kelly, J. T., Ku, I. T., McNeill, V. F., Riemer, N., Schaefer, T.,
1058   Shi, G., Tilgner, A., Walker, J. T., Wang, T., Weber, R., Xing, J., Zaveri, R. A., and Zuend, A.: The acidity of
1059   atmospheric particles and clouds, Atmospheric Chemistry and Physics, 20, 4809-4888,
1060   https://doi.org/10.5194/acp-20-4809-2020, 2020.

1061 Rahn, D. A. and Parish, T. R.: Diagnosis of the forcing and structure of the coastal jet near Cape Mendocino using in
1062   situ observations and numerical simulations, Journal of Applied Meteorology and Climatology, 46, 1455-1468,
1063   https://doi.org/10.1175/JAM2546.1, 2007.

1064 Rahn, D. A. and Parish, T. R.: Cessation of the 22–25 June 2006 coastally trapped wind reversal, Journal of Applied
1065   Meteorology and Climatology, 49, 1412-1428, https://doi.org/10.1175/2010JAMC2242.1, 2010.

1066 Ralph, F. M., Armi, L., Bane, J. M., Dorman, C., Neff, W. D., Neiman, P. J., Nuss, W., and Persson, P. O. G.:
1067   Observations and analysis of the 10–11 June 1994 coastally trapped disturbance, Monthly Weather Review, 126,
1068   2435-2465, https://doi.org/10.1175/1520-0493(1998)126<2435:OAAOTJ>2.0.CO;2, 1998.

1069 Reason, C. J. C. and Jury, M. R.: On the generation and propagation of the southern African coastal low, Quarterly
1070   Journal of the Royal Meteorological Society, 116, 1133-1151, https://doi.org/10.1002/qj.49711649507, 1990.

1071 Reason, C. J. C., Tory, K. J., and Jackson, P. L.: Evolution of a southeast Australian coastally trapped disturbance,
1072   Meteorology and Atmospheric Physics, 70, 141-165, https://doi.org/10.1007/s007030050031, 1999.

1073 Reid, H. J. and Leslie, L. M.: Modeling coastally trapped wind surges over Southeastern Australia. Part I: Timing
1074   and speed of propagation, Weather and Forecasting, 14, 53-66, https://doi.org/10.1175/1520-
1075   0434(1999)014<0053:MCTWSO>2.0.CO;2, 1999.

1076 Rogerson, A. M. and Samelson, R. M.: Synoptic forcing of coastal-trapped disturbances in the marine atmospheric
1077   boundary layer, Journal of Atmospheric Sciences, 52, 2025-2040, https://doi.org/10.1175/1520-
1078   0469(1995)052<2025:SFOCTD>2.0.CO;2, 1995.

1079 Rolph, G., Stein, A., and Stunder, B.: Real-time Environmental Applications and Display sYstem: READY,
1080   Environmental Modelling & Software, 95, 210-228, https://doi.org/10.1016/j.envsoft.2017.06.025, 2017.

1081 Russell, L. M., Sorooshian, A., Seinfeld, J. H., Albrecht, B. A., Nenes, A., Ahlm, L., Chen, Y.-C., Coggon, M.,
1082   Craven, J. S., Flagan, R. C., Frossard, A. A., Jonsson, H., Jung, E., Lin, J. J., Metcalf, A. R., Modini, R.,
1083   Mülmenstädt, J., Roberts, G., Shingler, T., Song, S., Wang, Z., and Wonaschütz, A.: Eastern Pacific Emitted
1084   Aerosol Cloud Experiment, Bulletin of the American Meteorological Society, 94, 709-729,
1085   https://doi.org/10.1175/bams-d-12-00015.1, 2013.

1086 Schlosser, J. S., Braun, R. A., Bradley, T., Dadashazar, H., MacDonald, A. B., Aldhaif, A. A., Aghdam, M. A., Mardi,
1087   A. H., Xian, P., and Sorooshian, A.: Analysis of aerosol composition data for western United States wildfires
1088   between 2005 and 2015: Dust emissions, chloride depletion, and most enhanced aerosol constituents, Journal of
1089   Geophysical Research: Atmospheres, 122, 8951-8966, https://doi.org/10.1002/2017jd026547, 2017.

1090 Schlosser, J. S., Dadashazar, H., Edwards, E.-L., Hossein Mardi, A., Prabhakar, G., Stahl, C., Jonsson, H.H., and
1091   Sorooshian, A.: Relationships between supermicrometer sea salt aerosol and marine boundary layer conditions:

1092   Insights from repeated identical flight patterns. Journal of Geophysical Research: Atmospheres, 125,
1093   e2019JD032346. https://doi.org/10.1029/2019JD032346, 2020.

1094   Skamarock, W. C., Rotunno, R., and Klemp, J. B.: Models of coastally trapped disturbances, Journal of the
1095   Atmospheric Sciences, 56, 3349-3365, https://doi.org/10.1175/1520-0469(1999)056<3349:MOCTD>2.0.CO;2,
1096   1999.

1097   Sorooshian, A., Wang, Z., Coggon, M. M., Jonsson, H. H., and Ervens, B.: Observations of sharp oxalate reductions
1098   in stratocumulus clouds at variable altitudes: Organic acid and metal measurements during the 2011 E-PEACE
1099   campaign, Environmental Science & Technology, 47, 7747-7756, https://doi.org/10.1021/es4012383, 2013.

1100   Sorooshian, A., MacDonald, A. B., Dadashazar, H., Bates, K. H., Coggon, M. M., Craven, J. S., Crosbie, E.,
1101   Edwards, E.-L., Hersey, S. P., Hodas, N., Lin, J. J., Mardi, A. H., Negrón Marty, A., Maudlin, L. C., Metcalf, A.
1102   R., Murphy, S. M., Padro, L. T., Prabhakar, G., Rissman, T. A., Schlosser, J. S., Shingler, T., Varutbangkul, V.,
1103   Wang, Z., Woods, R. K., Chuang, P. Y., Nenes, A., Jonsson, H. H., Flagan, R. C., Seinfeld, J. H., and Stahl, C.: A
1104   multi-year data set on aerosol-cloud-precipitation-meteorology interactions for marine stratocumulus clouds,
1105   Figshare, https://doi.org/10.6084/m9.figshare.5099983.v11, 2017.

1106   Sorooshian, A., MacDonald, A. B., Dadashazar, H., Bates, K. H., Coggon, M. M., Craven, J. S., Crosbie, E., Hersey,
1107   S. P., Hodas, N., Lin, J. J., Negrón Marty, A., Maudlin, L. C., Metcalf, A. R., Murphy, S. M., Padró, L. T.,
1108   Prabhakar, G., Rissman, T. A., Shingler, T., Varutbangkul, V., Wang, Z., Woods, R. K., Chuang, P. Y., Nenes, A.,
1109   Jonsson, H. H., Flagan, R. C., and Seinfeld, J. H.: A multi-year data set on aerosol-cloud-precipitation-
1110   meteorology interactions for marine stratocumulus clouds, Scientific Data, 5, 180026,
1111   https://doi.org/10.1038/sdata.2018.26, 2018.

1112   Sorooshian, A., Anderson, B., Bauer, S. E., Braun, R. A., Cairns, B., Crosbie, E., Dadashazar, H., Diskin, G.,
1113   Ferrare, R., Flagan, R. C., Hair, J., Hostetler, C., Jonsson, H. H., Kleb, M. M., Liu, H., MacDonald, A. B.,
1114   McComiskey, A., Moore, R., Painemal, D., Russell, L. M., Seinfeld, J. H., Shook, M., Smith, W. L., Thornhill,
1115   K., Tselioudis, G., Wang, H., Zeng, X., Zhang, B., Ziemba, L., and Zuidema, P.: Aerosol–cloud–meteorology
1116   interaction airborne field investigations: Using lessons learned from the U.S. West Coast in the design of
1117   ACTIVATE off the U.S. east coast, Bulletin of the American Meteorological Society, 100, 1511-1528,
1118   https://doi.org/10.1175/bams-d-18-0100.1, 2019.

1119   Stahl, C., Cruz, M. T., Bañaga, P. A., Betito, G., Braun, R. A., Aghdam, M. A., Cambaliza, M. O., Lorenzo, G. R.,
1120   MacDonald, A. B., Hilario, M. R. A., Pabroa, P. C., Yee, J. R., Simpas, J. B., and Sorooshian, A.: Sources and
1121   characteristics of size-resolved particulate organic acids and methanesulfonate in a coastal megacity: Manila,
1122   Philippines, Atmospheric Chemistry and Physics, 20, 15907-15935, https://doi.org/10.5194/acp-20-15907-2020,
1123   2020.

1124   Stein, A. F., Draxler, R. R., Rolph, G. D., Stunder, B. J. B., Cohen, M. D., and Ngan, F.: NOAA's HYSPLIT
1125   atmospheric transport and dispersion modeling system, Bulletin of the American Meteorological Society, 96,
1126   2059-2077, https://doi.org/10.1175/BAMS-D-14-00110.1, 2015.

1127   Thompson, W. T., Burk, S. D., and Lewis, J.: Fog and low clouds in a coastally trapped disturbance, Journal of
1128   Geophysical Research: Atmospheres, 110, https://doi.org/10.1029/2004jd005522, 2005.

1129   Twomey, S.: Pollution and the planetary albedo, Atmospheric Environment (1967), 8, 1251-1256,
1130   https://doi.org/10.1016/0004-6981(74)90004-3, 1974.

1131   Wang, Z., Sorooshian, A., Prabhakar, G., Coggon, M. M., and Jonsson, H. H.: Impact of emissions from shipping,
1132   land, and the ocean on stratocumulus cloud water elemental composition during the 2011 E-PEACE field
1133   campaign, Atmospheric Environment, 89, 570-580, https://doi.org/10.1016/j.atmosenv.2014.01.020, 2014.

1134   Wang, Z., Mora Ramirez, M., Dadashazar, H., MacDonald, A. B., Crosbie, E., Bates, K. H., Coggon, M. M., Craven,
1135   J. S., Lynch, P., Campbell, J. R., Azadi Aghdam, M., Woods, R. K., Jonsson, H., Flagan, R. C., Seinfeld, J. H.,
1136   and Sorooshian, A.: Contrasting cloud composition between coupled and decoupled marine boundary layer

1137   clouds, Journal of Geophysical Research: Atmospheres, 121, 11,679-611,691,
1138   https://doi.org/10.1002/2016jd025695, 2016.

1139   Watson, J. G., Chow, J. C., Lowenthal, D. H., Pritchett, L. C., Frazier, C. A., Neuroth, G. R., and Robbins, R.:
1140   Differences in the carbon composition of source profiles for diesel- and gasoline-powered vehicles,
1141   Atmospheric Environment, 28, 2493-2505, https://doi.org/10.1016/1352-2310(94)90400-6, 1994.

1142   Winant, C. D., Beardsley, R. C., and Davis, R. E.: Moored wind, temperature, and current observations made during
1143   Coastal Ocean Dynamics Experiments 1 and 2 over the Northern California Continental Shelf and upper slope,
1144   Journal of Geophysical Research: Oceans, 92, 1569-1604, https://doi.org/10.1029/JC092iC02p01569, 1987.

1145   Wood, R.: Stratocumulus clouds, Monthly Weather Review, 140, 2373-2423, https://doi.org/10.1175/mwr-d-11-
1146   00121.1, 2012.

1147   Wu, J.: Bubble flux and marine aerosol spectra under various wind velocities, Journal of Geophysical Research:
1148   Oceans, 97, 2327-2333, https://doi.org/10.1029/91JC02568, 1992.